Immuno-Based Molecular Scaffolding of Glucose Dehydrogenase and Ferrocene Mediator on *fd* Viral Particles Yields Enhanced Bioelectrocatalysis

Kristian Torbensen,[†] Anisha N. Patel,[†] Agnès Anne,*,[†] Arnaud Chovin,[†] Christophe Demaille,*,[†] Laure Bataille,[‡] Thierry Michon,*,[‡] and Eric Grelet[§]

[†]Laboratoire d'Electrochimie Moléculaire, Université Paris Diderot, Sorbonne Paris Cité, Unité Mixte de Recherche Université — UMR 7591 CNRS, Bâtiment Lavoisier, 15 Rue Jean-Antoine de Baïf, 75205 CEDEX 13 Paris, France

[‡]UMR 1332 Biologie du Fruit et Pathologie, INRA, Université de Bordeaux, 71, Avenue Edouard Bourlaux, CS 20032-33882 CEDEX Villenave d'Ornon, France

[§]Centre de Recherche Paul-Pascal, UMR 5031 CNRS, Université de Bordeaux, 115 Avenue Schweitzer, 33600 Pessac, France

S *Supporting Information*

ABSTRACT: A virus-based nanostructuring strategy is proposed for improving the catalytic performance of integrated redox enzyme electrodes. Random arrays of adsorbed filamentous *fd* bacteriophage particles, used as scaffolds, are assembled onto gold electrode surfaces. The viral particles are endowed with functionally coupled enzymatic and redox properties, by the sequential immunological assembly of quinoprotein glucose dehydrogenase conjugated antibodies and ferrocene PEGylated antibodies on their protein shell. The resulting virus-scaffolded enzyme/redox mediator integrated system displays a large enhancement in the catalytic current generated per enzyme molecule (i.e., in enzymatic turnover) as compared with nonscaffolded integrated glucose oxidizing enzyme electrodes. The mechanism underlying the observed scaffolding-induced catalytic enhancement is deciphered. Confinement of the mediator on the viral scaffold enables fast electron transport rate and shifts the enzyme behavior into its most effective cooperative kinetic mode.

KEYWORDS: bioelectrocatalysis, enzyme nanocarriers, bioelectrocatalytic viral particles, pyrroloquinoline quinone-dependent glucose dehydrogenase, bioscaffolding
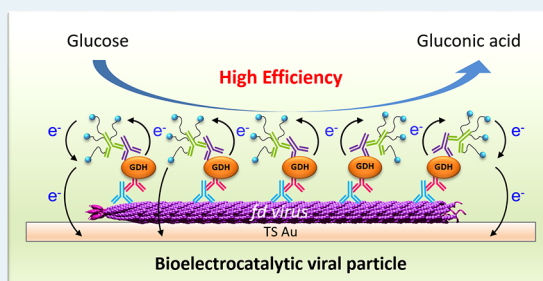
INTRODUCTION

Enhancing the catalytic activity of electrode-immobilized glucose oxidizing enzymes is key to the design of more sensitive glucose biosensors and more powerful biofuel cell anodes.[1,2] Glucose oxidase (GOx) and the much more active and oxygen-insensitive pyrroloquinoline quinone (PQQ)-dependent glucose dehydrogenase (PQQ-GDH) are among the most widely used redox enzymes for these important applications. A promising way to enhance their bioelectrocatalytic activity is to immobilize these enzymes on nanostructured electrode surfaces.[3−7] The expectation is that mastering the surface architecture at the nanometer scale will provide a more enzyme friendly environment, avoiding immobilization-induced denaturation. In addition, this may also improve the electrical communication between the redox enzymes and the electrode, notably if the enzyme can undergo direct electron transfer (DET) with the electrode material.[6,7] Similarly, for *integrated* systems,[8] where the enzyme and its redox mediator are coimmobilized onto the electrode surface, nanostructuring can enhance the rate at which the mediator shuttles electrons from the electrode to the enzyme.

In seminal works regarding integrated systems, the catalytic activity of nanostructured electrode materials combined with hydrogel composites entrapping both enzymes and redox centers has been assessed.[9−11] It has notably been shown that depositing GOx-containing redox hydrogels on carbon nanotubes microfiber networks, instead of on regular (non-nanostructured) carbon fibers, resulted in biofuel anodes displaying increased power density.[9] An enhanced catalytic response was also observed by "doping" with gold nanoparticles the electron conductivity of GOx containing redox-hydrogels.[10,11] Other works considered carbon nanotubes[12−14] and ZnO nanoparticles[15] functionalized by ferrocene moieties as redox mediators for polymer-entrapped GOx. Another type of nanostructured integrated system, consisting of a mesoporous enzyme electrode, where ferrocene molecules were trapped in nanopores capped with GOx, was also described.[16] Recently, PQQ-GDH has been covalently functionalized by a
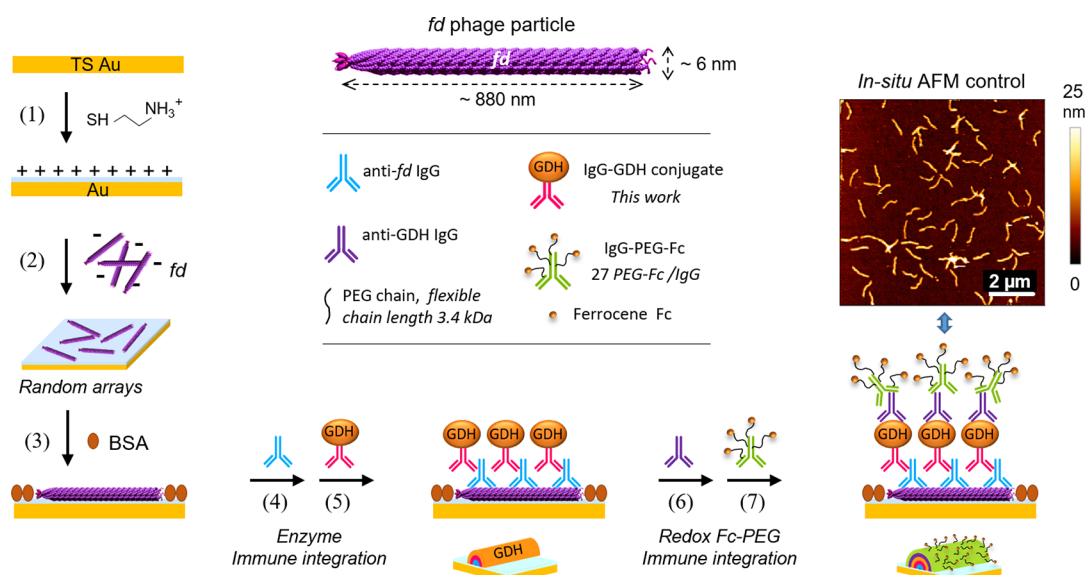
Figure 1. Assembly steps of the *fd*-scaffolded ferrocene-PEG-(Fc-PEG)/PQQ-GDH integrated system on a TS ultraflat gold electrode surface. Right: In situ AFM topography control image of a random array of Fc-PEG/PQQ-GDH immunodecorated *fd* particles on gold.

ferrocene mediator and immobilized on a quantum-dot-decorated electrode, and a photoelectrocatalytic response was evidenced.[17]

In search of nanostructures offering a microenvironment potentially more enzyme-favorable than inorganic nanoparticles or porous electrodes, integrated systems based on DNA material have been developed.[18−20] DNA hydrogels, incorporating GOx and a ferrocene mediator, have notably been reported.[18] DNA strands were also used as bioscaffolds to assemble GOx and ferrocene relays.[19,20]

Even though many of the above works reported valuable results, new nanostructuring or scaffolding strategies have to be designed to improve further the catalytic performances of integrated enzyme electrodes. This is evidenced by the fact that, for every integrated system reported in the literature, the apparent enzymatic turnover (i.e., the current generated per enzyme molecule) falls behind the turnover of the enzymes in solutions. This may result from the electron transport between redox relays being rate limiting or from partial inactivation of the enzyme.

In that context, the aim of our work is to explore the possibility of using an original bottom-up scaffolding approach for improving the catalytic performances of electrode-supported glucose oxidizing enzymatic systems. This strategy makes use of viral particles as electrode-immobilized bioscaffolds. The specific interest of using virus particles arises from their availability as perfectly monodisperse nanometer-sized particles and their highly ordered architectures enabling the topologically controlled assembly of enzyme molecules. Moreover, since the introduction of the concept of using viral particles as enzyme nanocarriers,[21,22] preserved or improved catalytic performances for virus-supported or virus-encapsulated enzymes, have been repeatedly reported, albeit almost exclusively for viral scaffolds dispersed *in solution*.[23−29] The possibility of using viral particles as enzyme carriers for enhancing the catalytic response of *electrode-supported* enzymatic systems has, at the opposite, been little explored. In pioneering works, Wege et al. reported that adsorbing GOx-functionalized tobacco mosaic virus nanotubes onto a sensor electrode surface did not actually enhance O_2-mediated

catalysis but significantly improved enzyme loading and sensor reusability.[30−32] The design of a bioanode bearing a random mesh of M13 bacteriophage particles decorated with GOx has also been reported, but in that case, the viral particles were "mineralized" by being gold coated in order to promote direct electron transfer (DET).[33]

Using an original immuno-based process, our group previously assembled a nonintegrated GOx-based system on *fd* bacteriophage particles adsorbed on gold electrodes.[34] What we address here is the benefit of scaffolding a much more complex, *integrated*, system on electrode-supported viral particles, by coimmobilizing a redox ferrocene mediator *and* the redox enzyme PQQ-GDH onto *fd* bacteriophage particles. Even though multienzymatic constructs on viral particles[30,35−37] and virus particles decorated by redox moieties have already been reported,[38−40] this is the first time that viral particles are endowed with functionally coupled redox *and* enzymatic properties.

Herein, *fd* particles, randomly adsorbed on a gold electrode surface, were equipped with redox and enzymatic functions thanks to the sequential immunological assembly of PQQ-GDH conjugated antibodies and redox-labeled antibodies on their protein shell (capsid). It is shown that confinement of the system's molecular components on the rod-like *fd*-nanoscaffold facilitates the mediated electronic communication between the enzyme and the supporting electrode, while fully preserving the enzyme activity, so that the electrocatalytic current is solely limited by the enzyme turnover rate. Moreover, confinement also results in shifting the PQQ-GDH kinetic behavior into its most effective cooperative mode. Consequently, the current generated by each of the GDH molecules incorporated in our *fd*-scaffolded system reaches exceptionally high values.

RESULTS AND DISCUSSION

Fd bacteriophage is a filamentous virus and a close cousin of the M13 bacteriophage, which is widely used to design virus-based biosensors.[41−43] *Fd* differs from M13 only by a single-point mutation of the 12th amino acid of each major coat protein, changing from asparagine (Asn) in M13 to aspartate (Asp) in *fd*. This results in a more negatively charged phage by
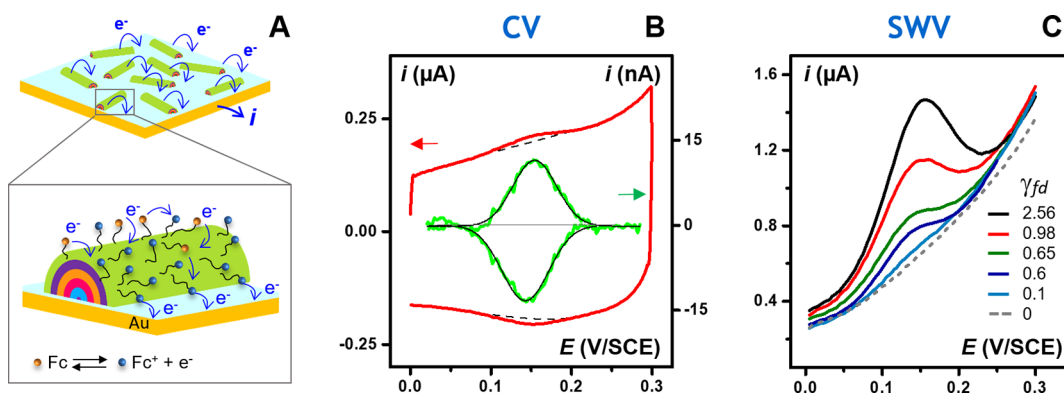
about 30%, having similar dimensions, 880 nm in length and 6.6 nm diameter (Figure 1). *Fd* bacteriophage can be used as an electroinactive rod-like enzyme *nano* carrier, which displays the extra advantages of being robust, easy to handle, and totally harmless to humans.

Step-by-Step Immunological Assembly of a PQQ-GDH Integrated System on *fd* Particles. *Fd* particles were adsorbed from a stock solution prepared in a 10 mM pH 7.4 phosphate buffer onto ultraflat template-stripped (TS) gold surfaces modified by a self-assembled layer of cysteamine (Figure 1).

As shown in our previous work, electrostatic attraction at pH 7.4 between the negatively charged *fd* particles and the positively charged cysteaminated gold surface results in the irreversible adsorption of *fd* on the surface to form random virus arrays.[34] Immediately following the adsorption of the *fd* particles, the surface was protected against nonspecific adsorption by a BSA backfilling step. The surface was then exposed to a rabbit antibody (immunoglobulin G, IgG) directed against the coat protein of *fd*, in order for this IgG to assemble by immunological recognition onto the whole virus capsid.

Then, the surface was sequentially exposed to a home prepared PQQ-GDH/antirabbit IgG conjugate, a commercial anti-GDH rabbit IgG, and finally to a redox-labeled antibody bearing polyethylene glycol (PEG) chains terminated by a ferrocene group (Fc).[44] Note that based on our previous experience of immunological assemblies,[45] we kept the concentration of the antibodies and the antigen−antibody reaction times high enough to ensure that a saturating "coating" of the virus particles by the IgGs was formed at every immunological immobilization step. This insures that a largely defect-free multimonolayer immunoconstruct is effectively assembled onto the virus capsid (see Supporting Information). Besides, as demonstrated earlier,[45] and confirmed here, the antigen−antibody binding was found to be strong enough to confer very high stability to the immunological assemblies (see Methods section). In situ AFM imaging of the surface allowed decorated *fd* particles, forming a random array on the gold surface, to be identified (Figure 1).

The virus coverage, γ_{fd}, was determined by simple counting of the viral particles visible in the AFM image. γ_{fd} was experimentally adjusted in the 0−2.5 *fd*/μm² range by controlling the concentration of the *fd* solution used for the adsorption step.

The redox and enzymatic integrated system ultimately assembled on the *fd* particles can, in principle, be schematically represented as shown in Figure 1. The successively assembled antibodies form concentric layers, color coded in Figure 1, around the virus scaffold. The expected "thickness" of each layer should correspond to the typical size of an IgG, ∼ 10 nm.[46] The enzymatic component of the system, the GDH enzyme, is considered as forming a layer of its own, the third layer, also of about ∼10 nm thickness.[47] The redox component of the system, the Fc-PEGylated antibody, comes as the last layer forming the outer "shell" of the assembly. Overall, the *fd* particles supporting the Fc-PEG/PQQ-GDH system should thus display a hemicylindrical geometry of ∼55 nm in radius and ∼900 nm in length.

We sought to experimentally confirm this schematic view of the *fd*-supported antibody construct by finely characterizing its

structure and/or functions by an ensemble of techniques, as described below.

We found that AFM imaging alone was not well-suited for monitoring the complete step-by-step assembly of the antibody construct on the *fd*-scaffold, as we observed that the height increment associated with the immobilization of antibody "layers" on the virus tended to become immeasurably small when more than three successive IgG layers were assembled. This result indicates that the multilayered antibody assembly on the virus is too soft to interact in a detectable way with the solid AFM tip.[48]

We thus turned to a more sophisticated local microscopy technique of our own,[49] combining AFM with scanning electrochemical microscopy (SECM) in an original mediator-tethered (Mt) configuration, for imaging individual virus particles decorated by the Fc-PEG/PQQ-GDH immunoconstruct. We previously demonstrated that this microscopy technique uniquely enabled mapping the distribution of redox functionalities on viral particles.[39]

Probing the Redox Function of the Decorated *fd* Particles at the Single Viral Particle Scale by Mt/AFM-SECM Microscopy. A homemade combined local probe (tip), acting as both a force sensor and a microelectrode, and operating in tapping mode, was used to raster scan the TS gold surface immersed in phosphate buffer. The probe and surface were biased at potentials, respectively, largely anodic (E_{tip} = +0.3 V/SCE) and cathodic (E_{sub} = −0.05 V/SCE) with respect to the standard potential of the Fc heads of the PEG chains (E^0 = 0.15 V/SCE). Simultaneously acquired topography and current Mt/AFM-SECM images of the surface are reproduced in Figure 2.

The topography images enabled identification and location of individual decorated *fd* particles and measurement of their apparent height (∼20 nm) and width (∼150 nm). These values are respectively under- and overestimates of the actual

Figure 2. Mt/AFM-SECM images of the individual decorated *fd* particles. Simultaneously recorded tapping-mode topography and tip current images. The contrast in the current image is generated by the electrochemical detection of the Fc heads by the scanning combined AFM-SECM probe (tip). Tip and TS gold surface potentials were, respectively, of E_{tip} = +0.3 V/SCE, E_s = −0.05 V/SCE. Scale bar: 200 nm. Imaging buffer: phosphate buffer.

Figure 3. (A) Schematic representation of the electron transfer and transport processes occurring at the gold electrode surface supporting a random array of *fd* particles decorated by the Fc-PEG/PQQ-GDH system, during the anodic scan of the electrode potential. (B) Cyclic voltammetry (CV) response of the gold electrode supporting an array of the decorated *fd* particles. The raw and background corrected CVs are plotted in red and green traces, respectively. Scan rate, 0.05 V/s. γ_{fd} = 2.56 *fd* particles/μm^2. (C) Square-wave voltammetry signal (SWV) of gold electrodes supporting decorated-*fd* particles at various coverages as indicated (in *fd* particles per μm^2). Medium: Tris buffer. SWV parameters: Amplitude, 25 mV; frequency, 25 Hz; increment, 5 mV.

particle dimensions because of tip−sample interactions and convolution artifacts common to all AFM-based imaging techniques. The current images showed electrochemical tip current detection specifically at the location of the particles. This current reflects the electrochemical probing of the Fc-heads by the tip. It is generated by electrons originating from the TS gold surface, propagating along the capsid of the decorated *fd* and ultimately collected by the tip, as schematized in Figure 2. Electron propagation over the few tens of nanometers high decorated virus particle is made possible by the swinging motion of the flexible PEG chains, coupled to electron exchange between neighboring Fc heads.[39,49,50] Importantly, no current was detected if decorated *fd* particles lacking the IgG-PEG-Fc were imaged or if the tip potential was less than the onset oxidation potential of the Fc heads.

These results demonstrate unambiguously the presence of Fc-PEG chains, hence of the Fc-PEG-IgG, on the capsid of the decorated *fd* particles. The observation that no current was recorded at locations on the surface away from the particles is an indication of the appropriate protection of the surface against nonspecific adsorption of the Fc-PEG-IgG. We also note that tip current was detected all along the length of the decorated *fd* particles, confirming that the immunoassembly covers the *entire* capsid of the *fd* particle. The fact that some sections of the *fd* particles appear as brighter spots in the current image may indicate the artifactual formation of antibody clusters resulting from the glutaraldehyde fixation of the sample, a required pretreatment step for Mt/AFM-SECM imaging (see Materials and Methods section). Finally, it is worth mentioning that all of the *fd* particles visible in topography images also appeared in the associated current images, showing that the immunological assembly process left no *fd* particles undecorated.

Even though we were able to visualize the Fc-PEG-IgG layer forming the outermost shell of the integrated virus-scaffolded assembly, extra characterization was needed in order to quantify the number of Fc-chains (hence of redox antibodies) decorating each *fd* particle. For this, we turned to cyclic voltammetry.

Quantifying the Number of Ferrocene Units Decorating *fd* Particles by Cyclic Voltammetry. Cyclic voltammograms (CVs) were recorded at gold surfaces bearing arrays of *fd* particles decorated by the Fc-PEG/PQQ-GDH system. The

surfaces were mounted in a liquid cell containing 50 mM Tris-HCl buffer pH 7.5 as the electrolyte. A typical raw CV signal, recorded at a potential scan rate of 0.05 V/s, is presented in Figure 3B (red trace).

The raw CV displays a pair of peaks superimposed on a large capacitive component that can be easily subtracted to yield the well-defined background-corrected signal shown in green trace in Figure 3B. On the corrected CV, the peak-shaped signal is centered on a potential of ~0.15 V/SCE, corresponding to the standard potential of the Fc heads, and the peak-to-peak potential separation is very small (~10 mV). Moreover, we verified that the intensity of the peaks was proportional to the scan rate, v (0.01−0.2 V/s range). All these characteristics evidence that the recorded CV signal corresponds to the response of surface confined Fc heads borne by the Fc-PEG-IgG of the construct, undergoing *fast* (Nernstian) electron transfer at the gold electrode surface.[51] As a result, integration of the anodic peak of the CV yields the surface coverage in Fc-PEG, Γ_{Fc}, which should depend on the number of decorated particles on the surface.

To verify this relationship, we carried out CV measurements for a large number of gold surfaces bearing decorated *fd* particles, randomly assembled at coverages varying from γ_{fd} = 0 (no *fd* particles) to 2.5 *fd* /μm^2. In parallel to CVs, we also recorded square wave voltammograms (SWVs) at these surfaces (Figure 3C). Indeed, SWV signals display a much lower background component than CVs, making it easier to probe the presence of the Fc heads from raw data (see Supporting Information). As seen in Figure 3C, the intensity of the SWVs was observed to increase with the virus coverage on the surface. The surface coverage in Fc heads, as determined by CV, obviously showed the same trend, as can be seen in Figure 4A, where experimental values of Γ_{Fc} (number of Fc/μm^2) are plotted as a function of γ_{fd}.

One can see that, at low coverages corresponding to γ_{fd} = 0−1.5 *fd* /μm^2, Γ_{Fc} increases linearly with γ_{fd}. Also, when no virus is present (γ_{fd} = 0), almost no Fc is detected, demonstrating the absence of nonspecifically adsorbed IgG-PEG-Fc on the surface. At high coverages, corresponding to γ_{fd} > 1.5 *fd* /μm^2, the Γ_{Fc} vs. γ_{fd} variation is seen to reach a plateau.

The linearity of the Γ_{Fc} vs γ_{fd} variation observed for γ_{fd} < 1.5 *fd* /μm^2 brings extra evidence that the Fc heads detected in CV and SWV are borne by the *fd* particles, and also shows that in
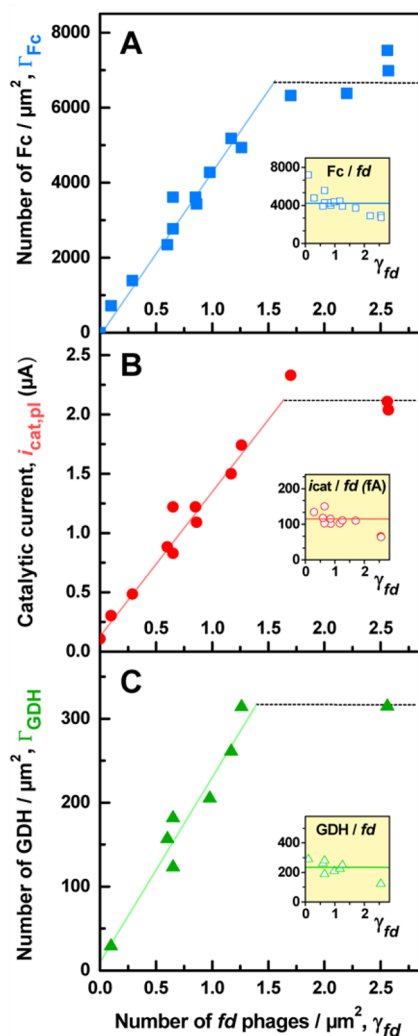
Figure 4. Structural and functional parameters characterizing gold surfaces bearing random arrays of *fd* particles decorated by the Fc-PEG/PQQ-GDH system, as a function of the *fd* surface coverage γ_{fd}. (A) Fc head surface coverage, Γ_{Fc} as determined by CV. (B) Intensity of the CV catalytic plateau current $i_{cat,pl}$ in Tris buffer containing 30 mM glucose. (C) GDH surface coverage as determined by the PQQ stripping method. The insets in (A), (B), and (C), respectively, show the number of Fc heads, the intensity of the catalytic plateau current and the number of GDH molecules per *fd* particle as a function of the *fd* coverage γ_{fd}.

this low γ_{fd} region the average number of Fc-PEG chains borne by decorated *fd*, N_{Fc}, does not vary with the virus coverage on the surface. N_{Fc} is given by the experimental Γ_{Fc}/γ_{fd} ratio, and is plotted as a function of γ_{fd} in the inset in Figure 4A. One can see that ~4000 ± 400 Fc heads are decorating each *fd* particle. Since each redox IgG used in this study bears ~24–30 Fc-PEG chains (see Materials and Methods section), one can conclude that as many as 120–180 IgG-PEG-Fc molecules are decorating each *fd* particles.

The observation of a plateau region in the Γ_{Fc} vs γ_{fd} plot, occurring beyond a threshold value of $\gamma_{fd} = 1.5$ *fd*/μm^2, indicates that at higher virus coverages on the gold surface, decoration of the *fd* particles becomes incomplete. As discussed in our previous work,[34] this can be attributed to the fact that, above this threshold, a significant fraction of the randomly adsorbed *fd* particles are intertwined and display

limited accessibility for the antibodies. As previously shown, this problem can be fully alleviated by orientating the *fd* particles, using simple molecular combing techniques.[34] However, being solely interested in exploring scaffolding effects, we did not attempt this here, and shall therefore only discuss data obtained with electrodes characterized by $\gamma_{fd} \leq 1.5$ *fd*/μm^2.

Having ascertained and quantified the selective redox-immunodecoration of the *fd* particles by the Fc-PEG chains, it is next necessary to evaluate the ability of the Fc heads to efficiently shuttle electrons from the gold surface toward the enzyme active site and to serve as enzymatic redox mediators.

Catalytic Activity of the Integrated Fc-PEG/PQQ-GDH System. Cyclic voltammetry was used to probe the catalytic activity of random arrays of *fd* particles decorated by the integrated Fc-PEG/PQQ-GDH system. To this aim, glucose was injected in the liquid cell holding the gold surface bearing the decorated *fd*-nanoarrays, and CVs were recorded at 10 mV/s.

As can be seen in Figure 5B, the injection of glucose resulted in a spectacular increase in intensity of the CV current, accompanied by a remarkable change in shape of the signal: from being dominated by the capacitive component (red trace), the current developed a marked S-shape (blue trace).

This change in shape is characteristic of the catalytic response of an integrated system, where both the mediator and the redox enzyme are immobilized on the electrode. In the present case and as schematically represented in Figure 5A, electrons resulting from the oxidation of glucose by GDH are transferred to nearby oxidized Fc heads (Fc$^+$), which play the role of enzymatic cofactors. Electrons are then relayed to the electrode surface by a composite charge transport process, implying physical elastic bounded motion of the Fc heads and electron self-exchanges between neighboring Fc/Fc$^+$ heads.[50] The high intensity and well-defined S-shape of the catalytic signal is thus a qualitative indication of the efficient coupling between electron transport and enzymatic catalysis in the *fd*-scaffolded immunoassembly.

As demonstrated earlier for integrated catalytic system,[52] in the absence of kinetic limitation due to electron transport, a catalytic voltammogram i_{cat} vs E, solely containing information on enzyme catalysis, can be conveniently obtained by subtracting the signal recoded in the absence of glucose from the catalytic signal obtained in its presence. The resulting subtracted signal plotted in Figure 5C displays a remarkably well-defined, hysteresis-free S shape, typical of purely catalytic voltammograms. This notably enables accurate determination of the catalytic plateau current, $i_{cat,pl}$.

Values of $i_{cat,pl}$ measured for several gold surfaces bearing decorated *fd* nanoarrays, characterized by differing virus coverages, are plotted as a function of γ_{fd} in Figure 4B. One can see that $i_{cat,pl}$ increases linearly with γ_{fd} up to $\gamma_{fd} \sim 1.5$ *fd*/μm^2 and reaches a plateau for higher γ_{fd} values. In the absence of viral particles ($\gamma_{fd} = 0$), a negligibly small catalytic current is recorded indicative of a trace amount of nonspecifically adsorbed IgG-PEG-Fc/IgG-GDH immunocomplexes on the electrode. These results evidence that the GDH molecules were specifically assembled on the virus capsid. The data presented in Figure 4B allow the average characteristic catalytic current generated by each individual *fd* particle, i_{fd}^{cat}, to be calculated from the expression: $i_{fd}^{cat} = i_{cat,pl}/(S\,\gamma_{fd})$, where S is the geometric surface area of the electrode. As seen in the inset in Figure 4B, a value of $i_{fd}^{cat} = 100 \pm 10$ fA per *fd* particle is
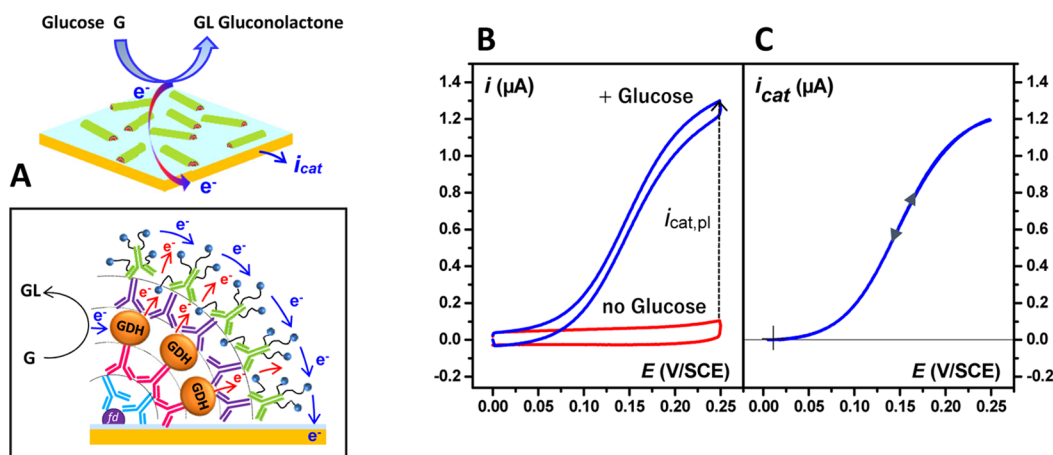
Figure 5. (A) Schematic representation of the catalytic oxidation of glucose by PQQ-GDH, coupled to electron transfer and transport processes occurring at the gold electrode surface supporting a random array of *fd* particles decorated by the Fc-PEG/PQQ-GDH system. (B) Cyclic voltammetry (CV) response of the gold electrode supporting a random array of decorated *fd* in the absence of glucose (red trace) and in the presence of 30 mM glucose (blue trace). (C) Purely catalytic voltammogram derived from the CVs presented in (B) by subtracting the CV recorded in the absence of glucose from the signal recorded in its presence. Scan rate, 0.01 V/s. γ_{fd} = 0.85 *fd* particles/μm^2. Medium: Tris buffer.

found for all of the surfaces examined, independently of their virus coverage.

Assaying the Number of GDH Enzyme Molecules Decorating the *fd* Particles. Our strategy for "counting" the number of GDH enzyme molecules decorating the *fd* particles is based on assaying the amount of its PQQ cofactor stripped from gold surfaces decorated by *fd*-nanorrays at various coverages of *fd* (see Supporting Information for details). For this, the surfaces were first treated by a 0.1 M pH 2.5 glycine buffer solution, in order to strip the antibodies off the viral scaffolds by disrupting antigen−antibody bonds. The recovered sample solution was then heated to 50 °C in order to trigger the spontaneous release of the noncovalently bound PQQ cofactors from GDH.[53] The concentration of PQQ in the heat-treated sample was then assayed by introducing in solution an excess of apo-GDH. The activity of the thus reconstituted holo-GDH enzyme in solution was finally monitored spectrophotometrically in the presence of glucose and soluble electron donors (see Supporting Information).[54,55]

The PQQ-GDH used herein is a dimer, each monomer containing one PQQ moiety. Hence, N_{total}^{GDH}, the amount of PQQ-GDH molecules initially present on the surface (i.e., on the *fd* particles), was derived simply by dividing the amount of assayed PQQ by a factor 2. The interest of this original protocol to quantify the amount of *fd*-immobilized PQQ-GDH is to be totally independent of the actual activity of the *fd*-bonded enzyme.

Figure 4C shows the value of the determined amount of PQQ-GDH, converted into an overall GDH coverage on the surface, $\Gamma_{GDH} = N_{total}^{GDH}/S$, and determined for a series of gold surfaces characterized by various γ_{fd} values. As can be seen, Γ_{GDH} increases linearly with γ_{fd} for $\gamma_{fd} < 1.5$ *fd*/μm^2, indicating that in this low γ_{fd} region, each *fd* particle carries on average $N_{fd}^{GDH} = \Gamma_{GDH}/\gamma_{fd} \sim 230 \pm 30$ GDH molecules, as shown in the inset.

The number of 230 GDH per *fd* particles found here is in fair agreement with the number of ~180 GOx molecules that, as shown previously, can be immunologically immobilized on randomly adsorbed *fd* particles.[34] Considering that the adsorbed *fd* particle exposes half of its total capsid area of 18 700 nm^2[56] and ~100 nm^2 as the footprint of an IgG, one

would expect that about 100 rabbit anti-*fd* IgG can bind to each *fd* particle. Since the antirabbit GDH conjugate is polyclonal, an estimate of 2−3 copies of it can thus possibly bind per anti-*fd* IgG, resulting in an estimated saturating number of 200−300 GDH molecules per *fd*. Hence it can be concluded that the packing density of GDH on the *fd* particles is close to its maximum; that is, the GDH-IgG conjugate forms a "saturating" layer on the virus capsid. This results confirms our previous observation,[22] and is in agreement with other works,[30,35,57] showing that affinity binding allows high yield decoration of virus particles by enzyme molecules.

Quantifying the Catalytic Efficiency of the Scaffolded Integrated System on the Basis of the Current Per Enzyme Molecule Parameter. Cross-analysis of the plots presented in Figure 4 enables deriving the $i_{fd}^{cat}/N_{fd}^{GDH}$ ratio, which is the value of the catalytic current generated by each GDH molecule incorporated in the *fd*-scaffolded integrated system, $i_{GDH}^{cat} = 0.45 \pm 0.09$ fA per GDH molecule. Remarkably, this specific current per enzyme molecule is 7 to 15 times higher than the 0.03−0.065 fA specific current that can be calculated for the most effective integrated PQQ-GDH system reported to date.[58]

This notable enhancement in specific current shows that electron transport, enzymatic activity, and/or their coupling is superiorly efficient in our virus-scaffolded Fc-PEG/PQQ-GDH system compared with all other reported integrated systems.

Note that the performances of integrated enzymatic systems are often discussed in terms of current density, rather than on the basis of the current generated per enzyme molecule as we do here (albeit the notion of current per mg of enzyme has been recently introduced for describing the performance of an enzymatic biofuel cell).[59] In order to achieve high current densities, it is quite common in the literature that the equivalent of several hundreds of enzyme monolayers are immobilized on an electrode, meaning that the suboptimal activity of the immobilized enzyme is artificially compensated by the enzyme loading of the system. We suggest that the current per enzyme criteria, as introduced here, is also used as a figure of merit for comparing integrated enzymatic systems, as it is a test of the ability of the entrapped enzyme to work at its optimal rate. Once optimal enzymatic conditions are
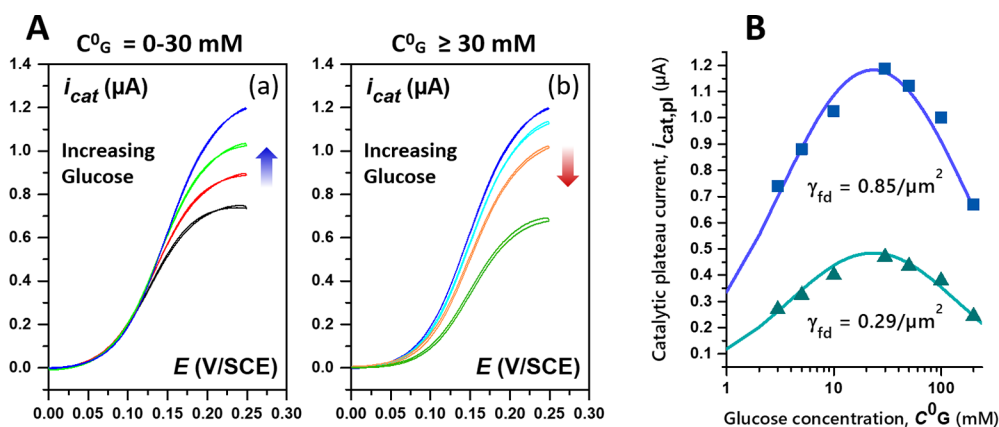
Figure 6. (A). Catalytic voltammograms recorded at a gold electrode bearing *fd* particles decorated by the PQQ-GDH integrated system in Tris buffer containing glucose at the following concentrations: (a) 3 (black), 5 (red), 10 (light green), 30 (blue) mM; (b) 30 (blue), 50 (cyan), 100 (orange), 200 (deep green) mM glucose. (B) Steady-state catalytic plateau currents $i_{cat,pl}$ as a function of glucose concentration C_g^0 for two surface coverages in decorated *fd* particles, γ_{fd}. Plain lines are the theoretical fits of eq 2 to the experimental data using the here-determined kinetic constants reported in Table 1. Scan rate ($v = 0.01$ V/s).

defined, high current densities can then be reached with minimal enzyme loading, which is obviously beneficial considering the cost of enzymes. More generally, expressing the performance of a catalytic system as a function of the amount of catalyst involved is common in the field of electrochemical catalysis,[60,61] but strangely enough, it is disregarded in the field of bioelectrocatalysis.

The all-protein microenvironnment experienced by the enzyme in the on-virus immunological assembly and the large enzyme-electrode separation probably contribute to make our virus-scaffolded integrated system so catalytically effective.[31,62] In order to reveal in more detail what are exactly the beneficial factors at play, a thorough kinetic analysis of its catalytic response was carried out by cyclic voltammetry.

Kinetic Analysis of the Catalytic Activity of GDH in the Virus-Scaffolded Integrated System. Cyclic voltammograms were recorded at a gold electrode bearing random arrays of *fd* particles immunodecorated by the Fc-PEG/PQQ-GDH system for increasing glucose concentrations. As seen in Figure 6A, it was observed that the plateau current of the catalytic signal increased in intensity with increasing glucose concentration, C_g^0, up to 30 mM, but then decreased when C_g^0 was further increased.

This behavior is indicative of the well-documented substrate inhibition of PQQ-GDH.[63,64] As a result, and as observed by others both for PQQ-GDH in solution,[64] or reconstituted as monolayers on electrode surface,[65] the variation of the catalytic plateau current, $i_{cat,pl}$, with the bulk glucose concentration, C_g^0, is bell-shaped, as seen in Figure 6B.

The kinetics of glucose oxidation catalyzed by the enzyme PQQ-GDH, using single electron ferrocene mediators as cosubstrates, has been studied in great details in literature.[64] From these studies, it appears that PQQ-GDH displays a very complex catalytic behavior characterized by the coexistence of two kinetic modes. A noncooperative mode, where no kinetic interaction exists between the monomers in the dimer constituting this enzyme (each monomer containing a PQQ active site), and a cooperative mode, where glucose binding by one of the monomeric units accelerates the catalytic action of the other. It was also shown that the noncooperative and cooperative modes were prevailing at low and high mediator concentrations, respectively. Later it was reported that, in

either of these modes, the stationary catalytic current generated by PQQ-GDH molecules confined on an electrode surface is given by the following expression:[65]

$$i_{cat} = \frac{2FS\Gamma_{GDH}}{\frac{1}{k_{ox}Q_0}(1 + K_iC_g^0) + \frac{1}{k_{cat}} + \frac{K_M}{k_{cat}C_g^0}} \quad (1)$$

where C_g^0 and Q_0 are, respectively, the bulk glucose concentration and the oxidized mediator concentrations locally "seen" by the enzyme. Observation of a well-defined plateau in the catalytic CVs ascertains that glucose consumption is negligible, so that C_g^0 can actually be taken as the bulk glucose concentration. k_{cat} is the catalytic constant of the enzyme, K_M the Michaelis constant for glucose, k_{ox} the second-order rate constant corresponding to the oxidation of the enzyme by the mediator, and K_i the equilibrium constant of the enzyme inhibition by glucose.

It was also shown that the individual values of the kinetic constants appearing in eq 1 differed greatly between the noncooperative and cooperative modes.

As reported previously,[52] for integrated systems, when neither electron transfer from the enzyme to the electrode nor electron transfer at the electrode limit the overall kinetics, Q_0 is simply given by the Nernst law. Q_0 is thus related to C_E^E, the total concentration of the mediator in both of its redox forms, and as "seen" by the enzyme, and also to the electrode potential E by

$$Q_0 = C_P^E/(1 + \exp(-F(E - E^0)/RT))$$

It thus appears legitimate to tentatively analyze the series of experimental catalytic voltammograms we recorded on the basis of eq 1, or more conveniently of its reciprocal expression:

$$1/i_{cat}(E) = \frac{1}{2FS\Gamma_{GDH}}\left\{\frac{[1 + \exp(-F(E - E^0)/RT)]}{k_{ox}C_P^E}\right.$$
$$\left.(1 + K_iC_g^0) + \frac{1}{k_{cat}}\left(1 + \frac{K_M}{C_g^0}\right)\right\} \quad (2)$$

which is actually a linearized theoretical expression for the catalytic voltammogram.
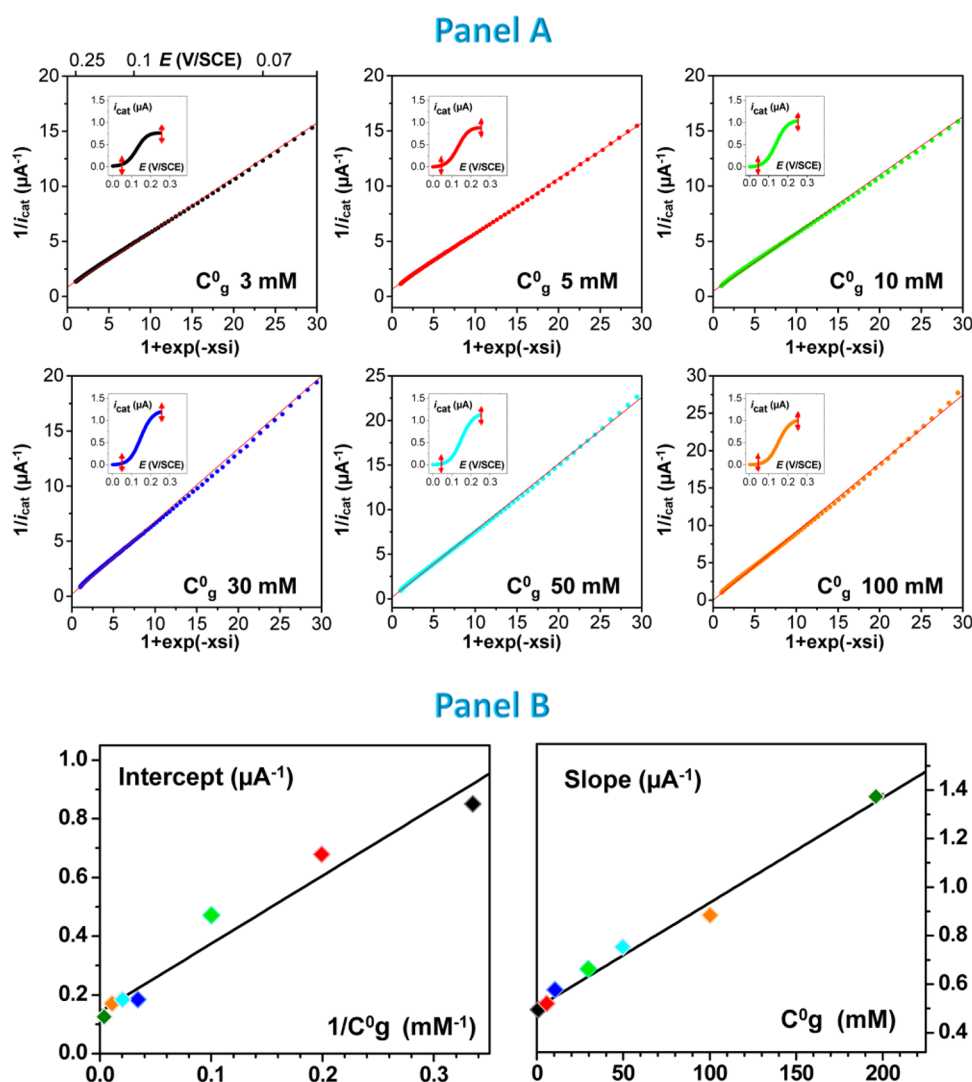
Panel A

Panel B

Figure 7. Kinetic analysis of the catalytic response of the integrated *fd*-scaffolded Fc-PEG/GDH system.(A) Primary plots where the reciprocal of the catalytic current ($i_{cat}(E)$) is plotted as a function of the $1 + \exp(-xsi)$ term calculated all along the voltammograms shown in the insets (in the electrode potential region delimited by the double-headed red arrow shown). Each plot corresponds to a different glucose concentration, C_g^0, as indicated. (B) Secondary plots showing the dependence of (left) the intercept of the primary plots with $1/C_g^0$ (right) the slope of the primary plots with C_g^0. Scan rate, 0.01 V/s. $\gamma_{fd} = 0.85$ *fd* particles/μm^2. Medium: Tris buffer.

Thus, as suggested by eq 2, we plotted reciprocal of the catalytic current i_{cat} (E), measured along the experimental catalytic voltammograms for a wide range of E values, as a function of the expression: $1 + \exp(-xsi)$, where $xsi = F(E - E_0)/(RT)$. As can be seen in Figure 7 panel A, and as predicted by eq 2, extremely well-defined linear variations were then obtained for all of the voltammograms recorded for various glucose concentrations, C_g^0.

Observation of such linear Lineweaver–Burk-like "primary plots" validates our analysis and initial assumptions. In particular, this result shows that in our integrated system, the overall kinetics of PQQ-GDH can be phenomenologically described by the kinetic eq 1, even though the kinetic mode adopted by GDH is not yet known.
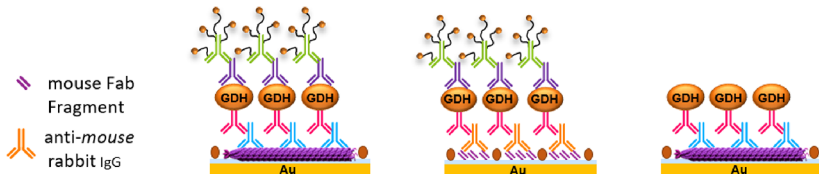
From eq 2, it can be seen that the theoretical expression for the slope, s_1, and origin, o_1, of the primary plots are respectively given by $s_1 = \dfrac{1 + K_i C_g^0}{2FS\Gamma_E k_{ox} C_P^0}$ and $o_1 = \dfrac{1 + K_M / C_g^0}{2FS\Gamma_E k_{cat}}$. Hence, the slopes of each of the lines shown in Figure 7 panel A were plotted as a function of the corresponding value of C_g^0, and their origins

were plotted as a function of $1/C_g^0$. As can be seen in Figure 7 panel B, two linear "secondary" plots were thus obtained, in agreement with theory.

Linear regression of the o_1 vs $1/C_g^0$ secondary plot (left plot in Figure 7 panel B), yielded best-fit values of $K_M = (14 \pm 2)$ mM and $k_{cat} = (8500 \pm 1100)$ s^{-1}. Similarly, linear fitting of the s_1 vs $1/C_g^0$ variation (right plot in Figure 7 panel B) yielded values of $K_i = (11 \pm 3)$ M^{-1} and $k_{ox}C_P^F = (3 \pm 0.7)$ 10^3 s^{-1}.

Determining the value of k_{ox} requires that the notion of the local concentration in mediator, C_P^F, is now clarified. C_P^F actually corresponds to the average local concentration in Fc heads as "seen" by the enzyme *active site*. Its value depends on the actual Fc-PEG coverage on the viral particles, on the respective positions of the IgG-PEG-Fc and GDH-IgG conjugate "layers" in the assembly, and also on the elasticity of the PEG chain. As discussed in detail in Supporting Information, a reasonable estimate for C_P^F can be obtained on the basis of our previously introduced elastic bounded diffusion model adapted to describe the behavior of IgG-bound Fc-PEG chains in

Table 1. Sets of Kinetic Constants and Specific Current per GDH Molecule Characterizing the Catalytic Activity of PQQ-GDH in Various Systems, Configurations, and Kinetic Modes As Indicated[a]

Enzymatic constants	(I) Integrated system GDH + Fc on *fd* Virus Nanoarray	(II) Integrated system GDH + Fc Monolayer	(III) Non-Integrated GDH on *fd* Fc in solution *Non-coop. mode*	(IV) GDH in solution[65] Fc in solution *Non-coop. mode*	(V) GDH in solution[65] Fc in solution *Coop. mode*
k_{ox} (10^{-7} M^{-1} s^{-1})	25 ± 6	1.4 ± 0.3	23 ± 4	19 ± 3.0	33 ± 6
k_{cat} (s^{-1})	8500 ± 1500	620 ± 300	1800 ± 300	1500 ± 300	6000 ± 1000
K_M (mM)	14 ± 2	1.7 ± 0.3	0.3 ± 0.1	0.27 ± 0.005	4.7 ± 0.3
K_i (M^{-1})	11 ± 3	6.2 ± 1.5	85 ± 20	52 ± 6	127 ± 20
Current / GDH molecule (fA)	**0.45**	**0.08**	**0.14**	-	-

[a]Columns (I) to (III) (gray background) present data derived herein on the basis of eq 1, and columns (IV) and (V) present data from ref 65.

immunoassemblies.[52] We thus derived a value of $C_P^F \sim 12$ μM, which yielded $k_{ox} = (2.5 \pm 0.6)$ 10^8 M^{-1} s^{-1}.

The set of values obtained here for k_{ox}, k_{cat}, K_M, and K_i for *fd*-scaffolded integrated system are gathered in Table 1 (Column (I)) and compared to those determined by Limoges et al. for PQQ-GDH, using ferrocene methanol as a mediator, and functioning in both of its kinetic modes in solution (Column (IV) and Column (V)).[65]

Comparing the data presented in Table 1, it appears that the values of both of the kinetic constants k_{ox} and k_{cat} measured for our *fd*-scaffolded integrated system match those corresponding to the cooperative mode of PQQ-GDH in solution. The value found here for K_m (14 ± 2 mM) is somewhat higher than that reported for the cooperative mode of PQQ-GDH (4.7 ± 0.3 mM), but mostly is ~20 times higher than the K_m value reported for the noncooperative mode of the enzyme. Interestingly, the value of the inhibition constant K_i we find for our system is ~10 and ~3 times lower than that reported for the cooperative and noncooperative modes, respectively.

Hence, our global observation of a particularly high activity of PQQ-GDH assembled on *fd*-nanoscaffolds can now be understood on the basis of enzyme kinetics: within our virus-scaffolded assembly, the conditions are such that the enzyme spontaneously adopts its cooperative mode. Besides, as an extra (less decisive) benefit, the *fd*-supported enzyme displays somewhat lower inhibition with respect to glucose than it does in its native state.

The simplest explanation for this unprecedented result is that the dense molecular arrangement of the IgG-PEG-Fc and GDH conjugated antibodies on the *fd*-scaffold, results in a local concentration in Fc heads sufficiently high to favor the cooperative mode of the enzyme. Actually, one can evaluate from the above data that each GDH molecule is, on average, surrounded by ~18 ± 5 Fc heads. The reason for a lower sensitivity to inhibition by glucose of the *fd*-scaffolded PQQ-GDH enzyme is not clear at this stage.

Demonstrating That Enhanced Bioelectrocatalysis Is Due to Scaffolding. In order to elucidate which part of these catalysis enhancing effects are due to confinement of the integrated system on the *fd*-scaffold, or to the particular molecular architecture of the immunological construct, we assembled the integrated system as an immunological *monolayer* on a planar gold surface (see scheme on top of Column (II) in Table 1). For this, the viral scaffold was replaced by a saturated monolayer of rabbit-Fab fragments, as they display approximately the same diameter (~5 nm)[46] as *fd* particles. We then fully characterized the catalytic response of the electrode. As can be read in Table 1, bottom line, the current per GDH molecule recorded for such system was only 0.08 fA (i.e., about 6 times lower than for the virus-scaffolded system). The kinetic constants derived from kinetic analysis were accordingly very low, even lower than expected for the noncooperative mode of GDH. This latter result indicates that when the system is assembled on a planar surface, the rate of electron transport, and not only GDH kinetics, contributes to the kinetic control of the catalytic current. Such is expected here since in a planar monolayer configuration, mere elongation of the 30 nm long fully extended PEG chains cannot allow the Fc$^+$-heads to directly collect electrons from the remote electrode surface. However, the fact that a catalytic current is nevertheless recorded suggests that hinge-like motion of the antibodies constituting the assembly provide an extra degree of freedom to the system, enabling electron transport from the enzyme to the electrode surface by electron hopping/elastic bounded diffusion.

The above comparative results demonstrate that the optimal catalytic response observed for the virus-scaffolded integrated system can unambiguously be attributed to a beneficial nanoscaffolding effect.

In search of the mechanism underlying such an effect, we assembled *a nonintegrated* two-IgG construct comprising solely the anti-*fd* antibody and the PQQ-GDH conjugate (see

Column (III) in Table 1), and we interrogated its activity by cyclic voltammetry, using ferrocene methanol as a soluble mediator. We restricted ourselves to a low concentration in mediator (3 μM), where the enzyme works in its non-cooperative mode, since previous work showed that for higher mediator concentrations, glucose diffusion partially controls the catalytic CV signals, which interferes with kinetic analysis.[65] The kinetic and thermodynamic constants we determined for the nonintegrated scaffolded system are reported in Table 1, Column (III). Comparing the data presented in Column (III) and Column (IV) shows that the activity of PQQ-GDH is virtually the same whether the enzyme is scaffolded on the *fd* particles or free in solution. This result confirms that the immunological assembly process fully preserves the activity of the enzyme, but also that scaffolding *by itself* does not enhance the catalytic performances of PQQ-GDH. Hence, we can conclude that the catalytic enhancement effect observed here for the integrated system is due to the confinement of *both* the enzyme *and* the redox mediator on the *fd*-scaffold. Our interpretation is that this effect is rooted in the nanoscale hemicylindrical geometry of the *fd*-scaffolded assembly which, as represented schematically in Figure 5A, facilitates access to the electrode for the Fc heads, but also accelerates electron transport within the assembly. This not only cancels the kinetic limitations due to electron propagation to/from the enzyme, but also, by ensuring a high local concentration in Fc heads in the vicinity of the enzymatic sites, it drives PQQ-GDH toward its most effective catalytic mode.

We believe that the present work is a rare example where the effect of enzyme nanoscaffolding could be so clearly evidenced and explained on sound enzyme kinetics and (nano)-topological basis. This is the first time that such an effect is evidenced for a fully integrated enzymatic system.

CONCLUSIONS

It has been shown herein that assembling an integrated enzymatic system on a viral nanoscaffold strongly enhances its catalytic performance compared to nonscaffolded systems. We elucidated the physical reason underlying such a catalytic improvement in the present case: the hemicylindrical arrangement of the system's molecular components on a nanometer-sized rod-like scaffold enhances the rate of mediated electronic communication between the enzyme and the supporting electrode. As a result, the only kinetic limitation to the current generated by the integrated system is enzyme kinetics. As a benefit of the enzyme-friendly microenvironment provided by the immunological assembly, the enzyme PQQ-GDH can remain fully active. Moreover, confinement of the Fc-PEG on the virus scaffold results in a high local mediator concentration, which shifts the enzyme behavior into its most effective cooperative mode. Consequently, the current generated by each of the GDH molecules incorporated in our *fd*-scaffolded system reaches its maximal, enzyme-kinetics-limited value, which significantly exceeds the current-per-enzyme molecule generated by other *integrated* PQQ-GDH systems reported in literature. More generally, we are not aware of any glucose oxidizing immobilized PQQ-GDH electrode where the enzyme was shown to work in its high-current-generating cooperative mode.

Although the present work is of a fundamental nature, it sets some rules for improving the performances of PQQ-GDH-integrated glucose biosensors and bioanodes, as we showed that optimal current-per-enzyme is achievable via virus particle-based nanostructuring of enzyme electrodes. However, for these applications, high current densities is also required, which is typically achieved in the literature by immobilizing the equivalent of multiple enzyme layers. Hence, a possible development of the present work would be forming multilayers of PQQ-GDH decorated *fd* particles, using for example layer-by-layer electrostatic assembly of *fd*/polyelectrolyte polymers,[66] to ensure both optimal enzyme activity and high current density.

MATERIALS AND METHODS

Biological Material. *Virus Particles.* Fd viruses were grown and purified as described elsewhere.[67] Virus suspensions were then concentrated by ultracentrifugation (200 000g) and redispersed in a stock solution of about 4 mg/mL as measured by spectrophotometry with an absorption coefficient of 3.84 cm^2/ mg at 269 nm. To control the ionic conditions, the fd suspension was then extensively dialyzed against 10 mM sodium phosphate buffer pH 7.4 and stored at 4 °C until further use.

Antibodies. The anti-*fd* polyclonal antibody (Immunoglobulin G, IgG) produced in rabbit was obtained from Sigma-Aldrich. The antirabbit GDH-IgG conjugate was prepared in-house by conjugating PQQ-GDH to a polyclonal goat antirabbit IgG, as detailed in Supporting Information. The anti-GDH polyclonal antibody was custom produced in rabbit by Genosphere Biotechnologies using apo-GDH monomers as antigens (see Supporting Information). The goat antirabbit antibody to be conjugated with GDH or Fc-PEG chains and the bovine serum albumin (BSA) (IgG-free grade) blocking agent were from Jackson ImmunoResearch Laboratories.

Enzymes. PQQ-GDH to prepare the IgG-GDH conjugate was produced from *Acinetobacter calcoaceticus* and purified as detailed in Supporting Information. Apo-GDH (GD-2) used for the PQQ assays was acquired form Sekisui enzymes.

Chemicals and Solutions. All chemicals were analytical-grade Sigma-Aldrich products and used as received, except for PQQ that was a gift from the group of Dr. Benoit Limoges. All solutions were prepared with double-deionized water (18.2 MΩ cm resistivity, TKA Micro-Pure UV). Two buffer solutions were used: 10 mM phosphate buffer at pH 7.4 (phosphate buffer), and 50 mM Tris-HCl buffer at pH 7.5. Phosphate buffer was used for the preparation of the *fd* bacteriophage solutions and the anti-*fd* antibody solutions employed for the assembly of the *fd*-scaffolded integrated system. Phosphate buffer was also the imaging medium for the in situ AFM and AFM-SECM experiments. Tris buffer was used to prepare the solutions of GDH-IgG conjugate, anti-GDH IgG, and Fc-PEG-IgG, which are required for the successive system assembly steps. Tris buffer was also the supporting electrolyte for the CV and SWV experiments. We chose Tris buffer over phosphate for these solutions/experiments since we observed increased stability of PQQ-GDH activity in Tris. All antibody solutions contained 1 mg/mL BSA. 0.01% sodium azide was added as a preservative to the antibody solutions if used or stored for longer than a few hours at room temperature. All solutions and systems were protected from light with aluminum foil during investigation and storage.

Preparation and Characterization of the Redox Secondary Antibody, IgG-PEG-Fc. Fc-PEG chains were covalently conjugated to goat antirabbit IgGs by reacting the NHS activated ester of a home synthesized NHS-PEG$_{3500}$-Fc

chain with the amino groups of the IgG species, as previously described.[44] The purified IgG-PEG-Fc product used in this study is decorated by a number of Fc-PEG molecules per IgG protein, $n \sim 27 \pm 3$, as determined by MALDI-TOF MS. Briefly, the IgG-PEG-Fc sample and its starting IgG were (after reconstitution in a 0.1 M ammonium acetate buffer) analyzed by MALDI-TOF MS on a UltrafleXtreme mass spectrometer (Bruker Daltonics). Sinapic acid (Aldrich) at a concentration of 45 mM in 50:50 water/acetonitrile (0.05% TFA) was used as a matrix. MALDI-TOF (positive ion mode) m/z data: *Starting IgG*, Singly charged ion M$^+$ 147121, Doubly charged ion M^{2+} 73179 —— *IgG-PEG Fc conjugate*, Singly charged ion M$^+$ 253 675 Doubly charged ion M^{2+} 126 337. Calculated M$^+$ for [IgG + **27.3** PEG$_{3500}$-Fc] $\sim$ 253 600 (knowing that the average molecular mass for the Fc-PEG$_{3500}$ chain is $\sim$3900).

Production of GDH, Preparation and Characterization of the GDH-IgG Conjugate. See Supporting Information.

Preparation of the Ultraflat Gold Electrodes. Ultraflat gold surfaces were produced by template-stripping of a 200 nm thick gold layer deposited on mica, as previously described.[68] A perforated Teflon adhesive mask was glued onto the surface in order to define a 4 mm diameter disk-shaped electrode. All subsequent surface modification steps were carried out by depositing/rinsing with $\sim$20 μL drops of solutions confined to the electrode area by the hydrophobic Teflon mask.

Preparation of Cysteaminated-Gold Surfaces. A 20 μL drop of a 5 mM cysteamine hydrochloride (HS-(CH$_2$)$_2$-NH$_3^+$, Cl$^-$) solution in water was left in contact with the electrode for 2 h under a water-saturated nitrogen atmosphere. The surface was then thoroughly rinsed by droplet replacement of cysteamine with water (twice) and then with phosphate buffer (twice). Drop replacement was cautiously carried out to avoid drying of the surface. Note, thiol-functionalized surfaces were kept under a water-saturated nitrogen atmosphere in all subsequent assembly steps to prevent oxidative desorption of the cysteamine layer from the gold surface.

Adsorption of Random *fd* Nanoarrays on Cysteaminated Gold. A 20 μL solution of phosphate buffer containing *fd* particles at 0.1 to 1.7 μg/mL ((0.4 to 7.0) $\times$ 10^{10} phage particles/mL) was deposited onto the cysteaminated gold surface for 5 min. The surface was then rinsed by two droplet replacement steps and left under phosphate buffer for 10 min for desorption of any weakly bound material.

Protective BSA Backfilling. *Fd*-bearing surfaces were backfilled with a protective BSA layer by adsorption from a 20 μL drop of 2 mg/mL BSA in phosphate for 1 h followed by two 10 min rinsing steps by drop replacement with phosphate buffer.

Assembly of the Anti-*fd* Antibody. The surface was left in contact for 1 h with a 20 μL droplet of a 2 μg/mL ($\sim$0.8 $\times$ 10^{13} molecules/mL) solution of the anti-*fd* rabbit antibody. After two 10 min drop replacement rinsing steps, the surface was stored overnight at room temperature in the dark under a phosphate buffer solution containing 1 mg/mL BSA and 0.01% (w/v) sodium azide. This overnight storage/desorption step was found to be important for reducing nonspecific binding of subsequent antibodies onto the surface.

Assembly of the PQQ-GDH Conjugated Antibody. A 20 μL droplet of a 5 μg/mL ($\sim$1.2 $\times$ 10^{13} molecules/mL) antirabbit GDH-IgG conjugate in Tris buffer was left in

contact with the surface for 2 h. Two drop replacement rinsing steps with Tris buffer containing 1 mg/mL BSA followed.

Assembly of the Anti-GDH Antibody. The surface was left in contact for 1 h with 20 μL of a 5 μg/mL solution of the rabbit anti-GDH IgG in Tris buffer. Rinsing was then carried out by drop replacement with Tris buffer containing 1 mg/mL BSA.

Assembly of the IgG-PEG-Fc Antibody. Twenty microliters of a 20 μg/mL solution of the prepared antirabbit IgG-PEG-Fc in Tris buffer were deposited on the surface, and the assembly reaction was left to proceed overnight at 4 °C.

When required, the surfaces were stored at 4 °C in Tris buffer and placed in a water-saturated nitrogen atmosphere.

Assaying the Amount of PQQ-GDH Molecules Immuno-Scaffolded on *fd* Particles. The assay protocol developed in this work is fully described in Supporting Information. Briefly, the antibodies of the immunoassembly are stripped off the *fd*-scaffolds, PQQ is thermally released from the IgG-GDH conjugate and assayed spectrophotometrically by an enzymatic method.

AFM Imaging. Tapping mode AFM images were acquired with a Nanowizard II microscope (JPK, Germany). In situ (i.e., in phosphate buffer) imaging was carried out with V-shaped contact mode probes (MLCT-AUMN or MSNL-10, Bruker, spring constant 0.1 N/m, tip curvature 20 nm).

AFM-SECM Imaging. Mt/AFM-SECM images were acquired using the JPK Nanowizard II microscope operated in AFM-SECM mode as previously described.[39] The AFM-SECM tips were hand-fabricated according to a procedure detailed elsewhere.[69] The standard JPK electrochemical liquid cell contained 900 μL of filtered phosphate buffer solution and was equipped with a platinum wire as a counter-electrode and a micro Ag/AgCl reference electrode. All potentials in this work are reported versus the KCl saturated calomel electrode reference SCE. A homemade bipotentiostat was used to control independently the potential applied to the TS gold surface and the electrochemical tip, as well as to measure the tip current. The tip current signal was passed through a 10 Hz low-pass analogue filter. The current images were first-order flattened, and a light Gaussian filter was applied. Images shown in text were processed using the JPK software.

Electrochemical Analysis. The surface was mounted in a standard JPK electrochemical liquid cell. Cyclic voltammograms (CVs) were recorded with a CHI630C electrochemical workstation, in a three-electrode configuration, using the platinum wire counter electrode encased in the JPK cell, and a standard KCl-saturated calomel electrode (SCE) inserted in the middle of the cell. Temperature of the air-conditioned room was around 22 °C. Measurements were carried out under ambient atmosphere because PQQ-GDH is insensitive to oxygen. Note, the stock solutions of glucose in Tris buffer were allowed to mutarotate overnight. When not in use, the electrodes bearing the Fc-PEG/PQQ-GDH system were stored at 4 °C in Tris buffer. When the electrodes had been stored for 1 week, a maximal loss of $\sim$15% in catalytic activity was typically observed.

■ ASSOCIATED CONTENT

ⓢ Supporting Information

The Supporting Information is available free of charge on the ACS Publications website at DOI: 10.1021/acscatal.9b01263.

Detailed experimental protocol for assaying the number of enzyme molecules borne by the viral particles; demonstration that the immunoassembly process yields saturated antibody layers onto the viral particles; correlation between the ferrocene head coverage on the electrodes, determined by CV, and the intensity of the corresponding SWV signals; estimation of the concentration of ferrocene heads "seen" by the enzyme; production of holo-GDH; and preparation and characterization of the GDH-IgG conjugate (PDF)

■ AUTHOR INFORMATION

Corresponding Authors
*E-mail: anne@univ-paris-diderot.fr.
*E-mail: demaille@univ-paris-diderot.fr.
*E-mail: thierry.michon@inra.fr.

ORCID
Christophe Demaille: 0000-0002-6393-6522
Eric Grelet: 0000-0002-9645-7077

Notes
The authors declare no competing financial interest.

■ REFERENCES

(1) Bollella, P.; Gorton, L. Enzyme Based Amperometric Biosensors. *Curr. Opin. Electrochem.* **2018**, *10*, 157−173.

(2) Meredith, M. T.; Minteer, S. D. Biofuel Cells: Enhanced Enzymatic Bioelectrocatalysis. *Annu. Rev. Anal. Chem.* **2012**, *5*, 157−179.

(3) Holzinger, M.; Le Goff, A.; Cosnier, S. Nanomaterials for Biosensing Applications: A Review. *Front. Chem.* **2014**, *2*, 63.

(4) Zhu, C.; Yang, G.; Li, H.; Du, D.; Lin, Y. Electrochemical Sensors and Biosensors Based on Nanomaterials and Nanostructures. *Anal. Chem.* **2015**, *87*, 230−249.

(5) Zhao, C.; Gai, P.; Song, R.; Chen, Y.; Zhang, J.; Zhu, J.-J. Nanostructured Material-Based Biofuel Cells: Recent Advances and Future Prospects. *Chem. Soc. Rev.* **2017**, *46*, 1545−1564.

(6) De Poulpiquet, A.; Ciaccafava, A.; Lojou, E. New Trends in Enzyme Immobilization at Nanostructured Interfaces for Efficient Electrocatalysis in Biofuel Cells. *Electrochim. Acta* **2014**, *126*, 104−114.

(7) Milton, R. D.; Wang, T.; Knoche, K. L.; Minteer, S. D. Tailoring Biointerfaces for Electrocatalysis. *Langmuir* **2016**, *32*, 2291−2301.

(8) Heller, A. Electrical Wiring of Redox Enzymes. *Acc. Chem. Res.* **1990**, *23*, 128−134.

(9) Gao, F.; Viry, L.; Maugey, M.; Poulin, P.; Mano, N. Engineering Hybrid Nanotube Wires for High-Power Biofuel Cells. *Nat. Commun.* **2010**, *1*, 2.

(10) Cortez, M. L.; Marmisollé, W.; Pallarola, D.; Pietrasanta, L. I.; Murgida, D. H.; Ceolín, M.; Azzaroni, O.; Battaglini, F. Effect of Gold Nanoparticles on the Structure and Electron-Transfer Characteristics of Glucose Oxidase Redox Polyelectrolyte-Surfactant Complexes. *Chem. - Eur. J.* **2014**, *20*, 13366−13374.

(11) Aquino Neto, S.; Milton, R. D.; Crepaldi, L. B.; Hickey, D. P.; De Andrade, A. R.; Minteer, S. D. Co-Immobilization of Gold Nanoparticles with Glucose Oxidase to Improve Bioelectrocatalytic Glucose Oxidation. *J. Power Sources* **2015**, *285*, 493−498.

(12) Callegari, A.; Cosnier, S.; Marcaccio, M.; Paolucci, D.; Paolucci, F.; Georgakilas, V.; Tagmatarchis, N.; Vázquez, E.; Prato, M. Functionalised Single Wall Carbon Nanotubes/Polypyrrole Composites for the Preparation of Amperometric Glucose Biosensors. *J. Mater. Chem.* **2004**, *14*, 807−810.

(13) Nazaruk, E.; Sadowska, K.; Biernat, J. F.; Rogalski, J.; Ginalska, G.; Bilewicz, R. Enzymatic Electrodes Nanostructured with Functionalized Carbon Nanotubes for Biofuel Cell Applications. *Anal. Bioanal. Chem.* **2010**, *398*, 1651−1660.

(14) Deng, L.; Liu, Y.; Yang, G.; Shang, L.; Wen, D.; Wang, F.; Xu, Z.; Dong, S. Molecular "Wiring" Glucose Oxidase in Supramolecular Architecture. *Biomacromolecules* **2007**, *8*, 2063−2071.

(15) Haddad, R.; Mattei, J. G.; Thery, J.; Auger, A. Novel Ferrocene-Anchored ZnO Nanoparticle/Carbon Nanotube Assembly for Glucose Oxidase Wiring: Application to a Glucose/Air Fuel Cell. *Nanoscale* **2015**, *7*, 10641−10647.

(16) Trifonov, A.; Herkendell, K.; Tel-Vered, R.; Yehezkeli, O.; Woerner, M.; Willner, I. Enzyme-Capped Relay-Functionalized Mesoporous Carbon Nanoparticles: Effective Bioelectrocatalytic Matrices for Sensing and Biofuel Cell Applications. *ACS Nano* **2013**, *7*, 11358−11368.

(17) Riedel, M.; Sabir, N.; Scheller, F. W.; Parak, W. J.; Lisdat, F. Connecting Quantum Dots with Enzymes: Mediator-Based Approaches for the Light-Directed Read-out of Glucose and Fructose Oxidation. *Nanoscale* **2017**, *9*, 2814−2823.

(18) Nguyen, K. V.; Holade, Y.; Minteer, S. D. DNA Redox Hydrogels: Improving Mediated Enzymatic Bioelectrocatalysis. *ACS Catal.* **2016**, *6*, 2603−2607.

(19) Piperberg, G.; Wilner, O. I.; Yehezkeli, O.; Tel-Vered, R.; Willner, I. Control of Bioelectrocatalytic Transformations on DNA Scaffolds. *J. Am. Chem. Soc.* **2009**, *131*, 8724−8725.

(20) Van Nguyen, K.; Giroud, F.; Minteer, S. D. Improved Bioelectrocatalytic Oxidation of Sucrose in a Biofuel Cell with an Enzyme Cascade Assembled on a DNA Scaffold. *J. Electrochem. Soc.* **2014**, *161*, H930−H933.

(21) Carette, N.; Engelkamp, H.; Akpa, E.; Pierre, S. J.; Cameron, N. R.; Christianen, P. C. M.; Maan, J. C.; Thies, J. C.; Weberskirch, R.; Rowan, A. E.; Nolte, R. J. M.; Michon, T.; Van Hest, J. C. M. A Virus-Based Biocatalyst. *Nat. Nanotechnol.* **2007**, *2*, 226−229.

(22) Cardinale, D.; Carette, N.; Michon, T. Virus Scaffolds as Enzyme Nano-Carriers. *Trends Biotechnol.* **2012**, *30*, 369−376.

(23) Minten, I. J.; Claessen, V. I.; Blank, K.; Rowan, A. E.; Nolte, R. J. M.; Cornelissen, J. J. L. M. Catalytic Capsids: The Art of Confinement. *Chem. Sci.* **2011**, *2*, 358−362.

(24) Aljabali, A. A. A.; Barclay, J. E.; Steinmetz, N. F.; Lomonossoff, G. P.; Evans, D. J. Controlled Immobilisation of Active Enzymes on the Cowpea Mosaic Virus Capsid. *Nanoscale* **2012**, *4*, 5640−5645.

(25) Patterson, D. P.; Schwarz, B.; El-Boubbou, K.; Van Der Oost, J.; Prevelige, P. E.; Douglas, T. Virus-like Particle Nanoreactors: Programmed Encapsulation of the Thermostable CelB Glycosidase inside the P22 Capsid. *Soft Matter* **2012**, *8*, 10158−10166.

(26) Pille, J.; Cardinale, D.; Carette, N.; Di Primo, C.; Besong-Ndika, J.; Walter, J.; Lecoq, H.; Van Eldijk, M. B.; Smits, F. C. M.; Schoffelen, S.; Van Hest, J. C. M.; Mäkinen, K.; Michon, T. General Strategy for Ordered Noncovalent Protein Assembly on Well-Defined Nanoscaffolds. *Biomacromolecules* **2013**, *14*, 4351−4359.

(27) Rurup, W. F.; Koay, M. S. T.; Cornelissen, J. J. L. M. Viruses as Model Nanoreactors to Study Enzyme Kinetics. In *Enzyme Nanocarriers*; Cardinale, D., Michon, T., Eds.; Taylor & Francis Group: New York, NY, 2015; pp 105−122.

(28) Cuenca, S.; Mansilla, C.; Aguado, M.; Yuste-Calvo, C.; Sánchez, F.; Sánchez-Montero, J. M.; Ponz, F. Nanonets Derived from Turnip Mosaic Virus as Scaffolds for Increased Enzymatic Activity of Immobilized Candida Antarctica Lipase B. *Front. Plant Sci.* **2016**, *7*, 464.

(29) Timmermans, S. B. P. E.; Van Hest, J. C. M. Self-Assembled Nanoreactors Based on Peptides and Proteins. *Curr. Opin. Colloid Interface Sci.* **2018**, *35*, 26−35.

(30) Koch, C.; Wabbel, K.; Eber, F. J.; Krolla-Sidenstein, P.; Azucena, C.; Gliemann, H.; Eiben, S.; Geiger, F.; Wege, C. Modified TMV Particles as Beneficial Scaffolds to Present Sensor Enzymes. *Front. Plant Sci.* **2015**, *6*, 1137.

(31) Bäcker, M.; Koch, C.; Eiben, S.; Geiger, F.; Eber, F.; Gliemann, H.; Poghossian, A.; Wege, C.; Schöning, M. J. Tobacco Mosaic Virus as Enzyme Nanocarrier for Electrochemical Biosensors. *Sens. Actuators, B* **2017**, *238*, 716−722.

(32) Koch, C.; Poghossian, A.; Schöning, M. J.; Wege, C. Penicillin Detection by Tobacco Mosaic Virus -Assisted Colorimetric Biosensors. *Nanotheranostics* **2018**, *2*, 184−196.

(33) Blaik, R. A.; Lan, E.; Huang, Y.; Dunn, B. Gold-Coated M13 Bacteriophage as a Template for Glucose Oxidase Biofuel Cells with Direct Electron Transfer. *ACS Nano* **2016**, *10*, 324−332.

(34) Patel, A. N.; Anne, A.; Chovin, A.; Demaille, C.; Grelet, E.; Michon, T.; Taofifenua, C. Scaffolding of Enzymes on Virus Nanoarrays: Effects of Confinement and Virus Organization on Biocatalysis. *Small* **2017**, *13*, 1603163.

(35) Patterson, D. P.; Schwarz, B.; Waters, R. S.; Gedeon, T.; Douglas, T. Encapsulation of an Enzyme Cascade within the Bacteriophage P22 Virus-like Particle. *ACS Chem. Biol.* **2014**, *9*, 359−365.

(36) Besong-Ndika, J.; Wahlsten, M.; Cardinale, D.; Pille, J.; Walter, J.; Michon, T.; Mäkinen, K. Towards the Reconstitution of a Two-Enzyme Cascade for Resveratrol Synthesis on Potyvirus Particles. *Front. Plant Sci.* **2016**, *7*, 89.

(37) Brasch, M.; Putri, R. M.; De Ruiter, M. V.; Luque, D.; Koay, M. S. T.; Caston, J. R.; Cornelissen, J. J. L. M. Assembling Enzymatic Cascade Pathways inside Virus-Based Nanocages Using Dual-Tasking Nucleic Acid Tags. *J. Am. Chem. Soc.* **2017**, *139*, 1512−1519.

(38) Steinmetz, N. F.; Lomonossoff, G. P.; Evans, D. J. Decoration of Cowpea Mosaic Virus with Multiple, Redox-Active, Organometallic Complexes. *Small* **2006**, *2*, 530−533.

(39) Nault, L.; Taofifenua, C.; Anne, A.; Chovin, A.; Demaille, C.; Besong-Ndika, J.; Cardinale, D.; Carette, N.; Michon, T.; Walter, J. Electrochemical Atomic Force Microscopy Imaging of Redox-Immunomarked Proteins on Native Potyviruses: From Subparticle to Single-Protein Resolution. *ACS Nano* **2015**, *9*, 4911−4924.

(40) Aljabali, A. A.; Barclay, J. E.; Butt, J. N.; Lomonossoff, G. P.; Evans, D. J. Redox-Active Ferrocene-Modified Cowpea Mosaic Virus Nanoparticles. *Dalt. Trans.* **2010**, *39*, 7569−7574.

(41) Mao, C.; Liu, A.; Cao, B. Virus-Based Chemical and Biological Sensing. *Angew. Chem., Int. Ed.* **2009**, *48*, 6790−6810.

(42) Peltomaa, R.; López-Perolio, I.; Benito-Peña, E.; Barderas, R.; Moreno-Bondi, M. C. Application of Bacteriophages in Sensor Development. *Anal. Bioanal. Chem.* **2016**, *408*, 1805−1828.

(43) Bhasin, A.; Ogata, A. F.; Briggs, J. S.; Tam, P. Y.; Tan, M. X.; Weiss, G. A.; Penner, R. M. The Virus Bioresistor: Wiring Virus Particles for the Direct, Label-Free Detection of Target Proteins. *Nano Lett.* **2018**, *18*, 3623−3629.

(44) Anne, A.; Demaille, C.; Moiroux, J. Elastic Bounded Diffusion. Dynamics of Ferrocene-Labeled Poly(Ethylene Glycol) Chains Terminally Attached to the Outermost Monolayer of Successively Self-Assembled Monolayers of Immunoglobulins. *J. Am. Chem. Soc.* **1999**, *121*, 10379−10388.

(45) Bourdillon, C.; Demaille, C.; Moiroux, J.; Savéant, J.-M. Step-by-Step Immunological Construction of a Fully Active Multilayer Enzyme Electrode. *J. Am. Chem. Soc.* **1994**, *116*, 10328−10329.

(46) Pease, L. F.; Elliott, J. T.; Tsai, D.-H.; Zachariah, M. R.; Tarlov, M. J. Determination of Protein Aggregation with Differential Mobility Analysis: Application to IgG Antibody. *Biotechnol. Bioeng.* **2008**, *101*, 1214−1222.

(47) Oubrie, A.; Rozeboom, H. J.; Kalk, K. H.; Duine, J. A.; Dijkstra, B. W. The 1.7 ÅCrystal Structure of the Apo Form of the Soluble Quinoprotein Glucose Dehydrogenase from Acinetobacter Calcoace-

ticus Reveals a Novel Internal Conserved Sequence Repeat. *J. Mol. Biol.* **1999**, *289*, 319−333.

(48) Kuznetsov, Y. G.; McPherson, A. Atomic Force Microscopy in Imaging of Viruses and Virus-Infected Cells. *Microbiol. Mol. Biol. Rev.* **2011**, *75*, 268−295.

(49) Anne, A.; Chovin, A.; Demaille, C.; Lafouresse, M. High-Resolution Mapping of Redox-Immunomarked Proteins Using Electrochemical-Atomic Force Microscopy in Molecule Touching Mode. *Anal. Chem.* **2011**, *83*, 7924−7932.

(50) Anne, A.; Demaille, C.; Moiroux, J. Elastic Bounded Diffusion and Electron Propagation: Dynamics of the Wiring of a Self-Assembly of Immunoglobulins Bearing Terminally Attached Ferrocene Poly-(Ethylene Glycol) Chains According to a Spatially Controlled Organization. *J. Am. Chem. Soc.* **2001**, *123*, 4817−4825.

(51) Laviron, E. General Expression of the Linear Potential Sweep Voltammogram in the Case of Diffusionless Electrochemical Systems. *J. Electroanal. Chem. Interfacial Electrochem.* **1979**, *101*, 19−28.

(52) Anicet, N.; Anne, A.; Bourdillon, C.; Demaille, C.; Moiroux, J.; Savéant, J. M. Electrochemical Approach to the Dynamics of Molecular Recognition of Redox Enzyme Sites by Artificial Cosubstrates in Solution and in Integrated Systems. *Faraday Discuss.* **2000**, *116*, 269−279.

(53) Witarto, A. B.; Ohtera, T.; Sode, K. Site-Directed Mutagenesis Study on the Thermal Stability of a Chimeric PQQ Glucose Dehydrogenase and Its Structural Interpretation. *Appl. Biochem. Biotechnol.* **1999**, *77*, 159−168.

(54) Shen, D.; Meyerhoff, M. E. Pyrroloquinoline Quinone-Doped Polymeric Nanospheres as Sensitive Tracer for Binding Assays. *Anal. Chem.* **2009**, *81*, 1564−1569.

(55) Zimmerman, L. B.; Lee, K. D.; Meyerhoff, M. E. Visual Detection of Single-Stranded Target DNA Using Pyrroloquinoline-Quinone-Loaded Liposomes as a Tracer. *Anal. Biochem.* **2010**, *401*, 182−187.

(56) Zimmermann, K.; Hagedorn, H.; Heuck, C. C.; Hinrichsen, M.; Ludwig, H. The Ionic Properties of the Filamentous Bacteriophages Pf1 and Fd. *J. Biol. Chem.* **1986**, *261*, 1653−1655.

(57) Grelet, E.; Rana, R. From Soft to Hard Rod Behavior in Liquid Crystalline Suspensions of Sterically Stabilized Colloidal Filamentous Particles. *Soft Matter* **2016**, *12*, 4621−4627.

(58) Flexer, V.; Mano, N. Wired Pyrroloquinoline Quinone Soluble Glucose Dehydrogenase Enzyme Electrodes Operating at Unprecedented Low Redox Potential. *Anal. Chem.* **2014**, *86*, 2465−2473.

(59) Mazurenko, I.; Monsalve, K.; Infossi, P.; Giudici-Orticoni, M. T.; Topin, F.; Mano, N.; Lojou, E. Impact of Substrate Diffusion and Enzyme Distribution in 3D-Porous Electrodes: A Combined Electrochemical and Modelling Study of a Thermostable H2/O2 Enzymatic Fuel Cell. *Energy Environ. Sci.* **2017**, *10*, 1966−1982.

(60) Costentin, C.; Savéant, J.-M. Towards an Intelligent Design of Molecular Electrocatalysts. *Nat. Rev. Chem.* **2017**, *1*, 0087.

(61) Voiry, D.; Chhowalla, M.; Gogotsi, Y.; Kotov, N. A.; Li, Y.; Penner, R. M.; Schaak, R. E.; Weiss, P. S. Best Practices for Reporting Electrocatalytic Performance of Nanomaterials. *ACS Nano* **2018**, *12*, 9635−9638.

(62) Bourdillon, C.; Demaille, C.; Gueris, J.; Moiroux, J.; Savéant, J.-M. A Fully Active Monolayer Enzyme Electrode Derivatized by Antigen-Antibody Attachment. *J. Am. Chem. Soc.* **1993**, *115*, 12264−12269.

(63) Olsthoorn, A. J. J.; Otsuki, T.; Duine, J. A. Negative Cooperativity in the Steady-State Kinetics of Sugar Oxidation by Soluble Quinoprotein Glucose Dehydrogenase from Acinetobacter Calcoaceticus. *Eur. J. Biochem.* **1998**, *255*, 255−261.

(64) Durand, F.; Limoges, B.; Mano, N.; Mavré, F.; Miranda-Castro, R.; Savéant, J. M. Effect of Substrate Inhibition and Cooperativity on the Electrochemical Responses of Glucose Dehydrogenase. Kinetic Characterization of Wild and Mutant Types. *J. Am. Chem. Soc.* **2011**, *133*, 12801−12809.

(65) Zhang, L.; Miranda-Castro, R.; Stines-Chaumeil, C.; Mano, N.; Xu, G.; Mavré, F.; Limoges, B. Heterogeneous Reconstitution of the PQQ-Dependent Glucose Dehydrogenase Immobilized on an

Electrode: A Sensitive Strategy for PQQ Detection down to Picomolar Levels. *Anal. Chem.* **2014**, *86*, 2257−2267.

(66) Yoo, P. J.; Nam, K. T.; Belcher, A. M.; Hammond, P. T. Solvent-Assisted Patterning of Polyelectrolyte Multilayers and Selective Deposition of Virus Assemblies. *Nano Lett.* **2008**, *8*, 1081−1089.

(67) Sambrook, J.; Fritsch, E. F.; Maniatis, T. *Molecular Cloning: A Laboratory Manual*; Cold Spring Harbor Laboratory Press: Cold Spring Harbor, New York, 1989.

(68) Huang, K.; Anne, A.; Bahri, M. A.; Demaille, C. Probing Individual Redox PEGylated Gold Nanoparticles by Electrochemical-Atomic Force Microscopy. *ACS Nano* **2013**, *7*, 4151−4163.

(69) Abbou, J.; Demaille, C.; Druet, M.; Moiroux, J. Fabrication of Submicrometer-Sized Gold Electrodes of Controlled Geometry for Scanning Electrochemical-Atomic Force Microscopy. *Anal. Chem.* **2002**, *74*, 6355−6363.

Supporting Information

Immuno-Based Molecular Scaffolding of Glucose Dehydrogenase and Ferrocene Mediator on *fd* Viral Particles Yields Enhanced Bioelectrocatalysis

Kristian Torbensen[1], Anisha N. Patel[1], Agnès Anne*[1], Arnaud Chovin[1], Christophe Demaille*[1],

Laure Bataille[2], Thierry Michon*[2]

Eric Grelet[3]

[1]Laboratoire d'Electrochimie Moléculaire, Université Paris Diderot, Sorbonne Paris Cité, Unité Mixte de Recherche Université – UMR 7591 CNRS , Bâtiment Lavoisier, 15 rue Jean-Antoine de Baïf, 75205 Paris Cedex 13, France

[2]UMR 1332 Biologie du Fruit et Pathologie, INRA, Université de Bordeaux, 71, avenue Edouard Bourlaux, CS 20032-33882 Villenave d'Ornon Cedex, France

[3]Centre de Recherche Paul-Pascal, UMR 5031 CNRS, Université de Bordeaux, 115 avenue Schweitzer, 33600 Pessac, France

* To whom correspondence should be addressed.

E-mail: anne@univ-paris-diderot.fr ; demaille@univ-paris-diderot.fr ; thierry.michon@inra.fr

(I) Correlation between the peak current of the square wave voltammetry signal (SWVs) and the ferrocene surface coverage Γ_{Fc}, as determined by cyclic voltammetry (CV).

For each of the surfaces bearing arrays of decorated *fd* particles, we recorded both CV and SWV in TRIS buffer. We derived the Fc coverage, Γ_{Fc}, by integrating the anodic peak of the background subtracted CVs, and also measured the peak current of the SWVs, $i_{p,swv}$. As seen in Figure S1, a linear correlation between $i_{p,swv}$ and Γ_{Fc} was observed.
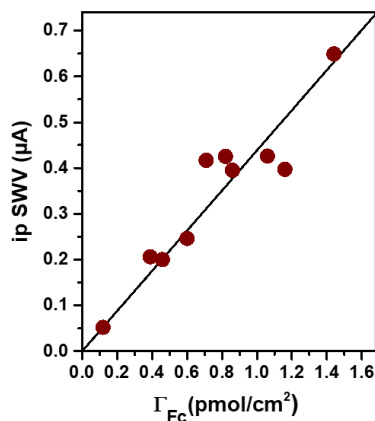
Figure S1. Correlation between the peak current of the square wave voltammetry signal (SWV), and ferrocene surface coverage Γ_{Fc} determined by cyclic voltammetry (CV). CVs and SWVs were recorded at gold electrodes bearing arrays of *fd*-decorated particles at differing virus coverages. Scan rate in CV $v = 0.05$ V/s, SWV parameters: amplitude, 25 mV; frequency, 25 Hz; increment 5 mV.

This correlation falls in line with the fact that the peak current of SWV for a surface-confined redox species is theoretically predicted to be proportional to the surface coverage of that species.[1] Yet, since no convenient analytical expression is available for SWV signals, we could not derive Γ_{Fc} from SWVs. The observed linear $i_{p,swv}$ vs. Γ_{Fc} correlation can however be seen as a positive self-consistency test, validating our measurement of Γ_{Fc} based on background-corrected CVs. This is particularly important for low Γ_{Fc} values where raw CV signals display a large, delicate to correct, capacitive background, whereas SWV signals display a much lower background.

(II) Relation between the amount of Fc heads decorating the *fd*-particles, and the number of antibodies in the immunoconstruct. Demonstrating the step-by-step assembly of saturated antibody layers.

The number of Fc heads borne by *fd*-scaffolds decorated by a two-layer antibody construct, consisting of the anti-capsid rabbit IgG and the anti-rabbit IgG-PEG-Fc, was determined by cyclic and square wave voltammetry, as described above (data not shown). For this particular construct we found a number of 1400 ± 150 Fc heads per virus particles, which is 2.9 ± 0.6 times less than for the full Fc-PEG / PQQ-GDH assembly. This difference in Fc coverage is due to the dissimilar sizes of the two constructs, translating into markedly different surface areas available for IgG-PEG-Fc binding. Considering the hemi-cylindrical geometry of the system, the surface accessible to the IgG-PEG-Fc is given by $S \sim \pi LR$, where L is the *fd*-length and R the radius of the assembly. Taking ~10 nm as the approximate diameter of both an IgG and of GDH, and ~ 5 nm as the virus radius, R can be estimated as 15 nm and 45 nm for the full and the two-IgG assemblies respectively. The number of IgG-PEG-Fc (hence of Fc heads) that any of these constructs can bear at saturation is simply expected to be proportional to S (i.e. to R), and is thus predicted to be *three times* higher for the full construct than for the two-layer assembly. This prediction is in quantitative agreement with the 2.9 ± 0.6 ratio in Fc heads we determined above for these systems. This result confirms the regular layer-by-layer growth of the

immunoassembly onto the *fd*-scaffold. It also shows that each of the assembled IgG layers is indeed saturated, and prevents insertion of antibodies into the underlying layers. As a result well-ordered, largely defect free, multi-monolayer constructs are obtained, as was demonstrated previously for planar immunoassemblies.[2]

(III) Assay of the total amount of GDH molecules immuno-scaffolded on viral capsids.

1- Stripping the antibodies from the *fd*-particles decorated by the enzyme system.

The immunological assembly was stripped from the virus capsid by letting a 20 μL drop of 0.1 M glycine buffer at pH 2.5 wet the electrode surface for 1.5 hour under a nitrogen atmosphere. The droplet was collected, and the surface was rinsed twice with two other droplets of 20 μL tris-HCl buffer at pH 7.5. All three droplets were pooled to obtain a ~60 μL sample, containing the stripped antibodies, and later to be assayed for its PQQ content. CV and SWV analysis of the surfaces revealed a complete loss of the Fc-PEG signal after stripping, as can be seen in Figure S2A, and Figure S2B, evidencing that the Fc-PEG-IgGs had been released from the surface. That the IgG-GDH conjugate was also stripped from the surface was verified by the complete loss of enzymatic activity after stripping, see Figure S2C.
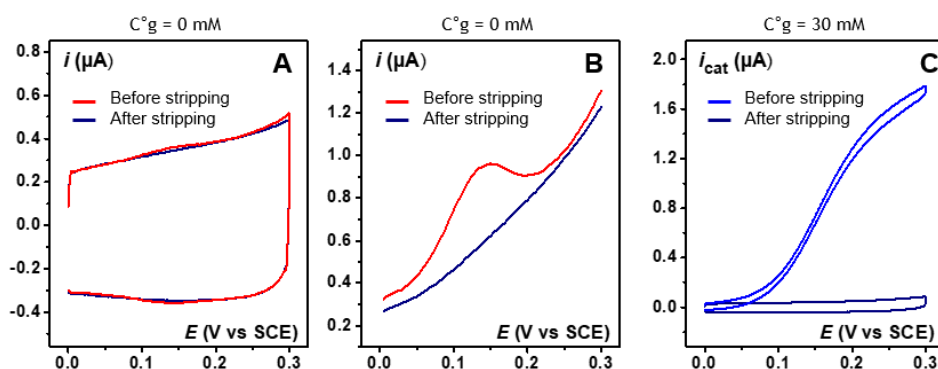
Figure S2. Stripping of the immunological assembly from the *fd*-scaffolds by the glycine buffer treatment. Comparisons of the signals recorded at a gold electrode bearing a random array of decorated *fd*-particles before and after the glycine treatment. (A) CV, and (B) SWV signals, recorded in Tris buffer. (C) CV catalytic signal recorded in Tris containing 30 mM glucose. $\gamma_{fd} = 0.78$ fd/μm^2. CV Scan rates: in (A) 0.1 V/s, in (C) 0.01 V/s. SWV parameters: amplitude, 25 mV; frequency, 25 Hz; increment 5 mV.

2- Thermal denaturation of GDH stripped-off from the decorated *fd*-particles.

The sample containing the stripped antibodies was brought to 100 μL by addition of 0.1 M pH 7.5 tris-HCL, and heated in a circulation water bath to 50°C for 1h. At this temperature, GDH is irreversibly denaturated,[3] and its PQQ cofactor is released.

3- Assaying the amount of PQQ released from the thermally denatured GDH.

The amount of PQQ thermally released form the GDH molecules in the sample, i.e. that originally decorated the *fd*-particles, was determined following a previously reported method.[4,5,6] This assay is based on measuring the activity of apo-GDH, added in excess to the sample, and reconstituted into its

active holo-GDH form by the PQQ to be assayed. To enable catalysis, glucose and two redox cofactors, phenazine methosulphate (PMS), and 2,6-dichlorophenolindophenol (DCPIP) are also added to the sample. DCPIP acts as the terminal electron acceptor of the catalytic system and its concentration decay is monitored spectrophotometrically.

In a cuvette, the following were mixed (the final concentrations in the total volume of 200 µL are indicated in parenthesis):

- The 100 µL heat-treated sample
- 70 µL 0.1 M pH 7.5 Tris-HCl (TB100)
- 10 µL DCPIP at 1 mM (50 µM) in TB100
- 10 µL PMS/Ca^{2+} at 20 mM (1 mM) in TB100
- 10 µL apo-GDH at 62.5 µg/mL (25 nM) in TB100
- 2 µL glucose solution at 0.5 M (5 mM) in TB100

Measurements of the absorbance of DCPIP at 605 nm was initiated immediately after addition of the glucose. Data points were acquired each 10 s for 600 s. A linear decay of absorbance was observed, as seen in Figure S3A.
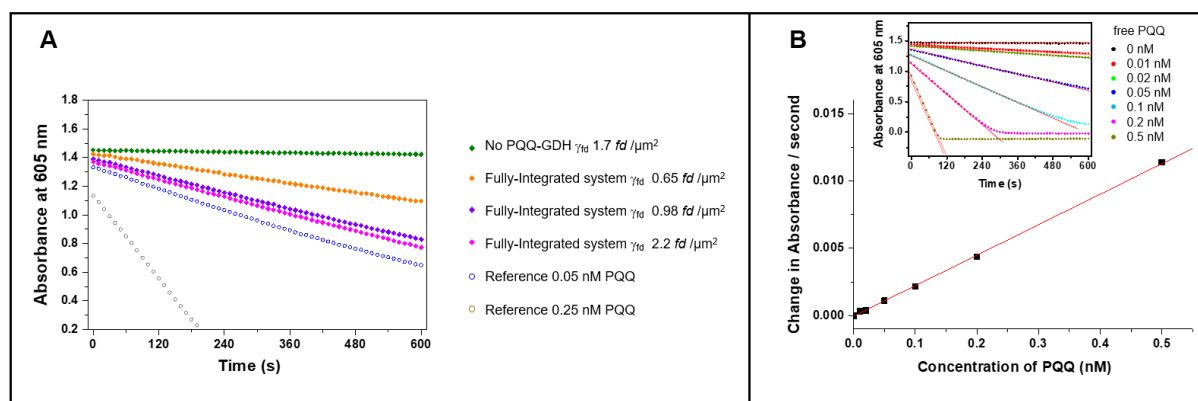
Figure S3. Spectrophotometry assay of PQQ. (A) Assay of PQQ contained in samples of antibodies stripped-off from gold surfaces bearing decorated *fd*-particles at various virus coverages, γ_{fd}. The plot shows the time decay of the absorbance at 605 nm resulting from the consumption of the DCPIP electron acceptor by the glucose oxidation reaction catalyzed by apo-GDH reconstituted in situ with the PQQ to be assayed. Note that the data point in green correspond to a surface bearing *fd*-particles decorated by the anti-*fd* rabbit IgG and the anti-rabbit IgG-PEG-Fc but missing the GDH conjugated IgG. (B) – Inset – Same decay plot as in (A) but for standard PQQ solutions. – Main graph – Calibration curve obtained by plotting the initial absorbance decay rate as a function of the PQQ concentration of the standard solutions.

As expected, and as can be seen in Figure S3A, the decay rate increased with the initial virus coverage on the electrode, γ_{fd}, i.e. with the amount of PQQ released form the surface. This rate, expressed in terms of absorbance loss per seconds, was converted into the actual PQQ concentration in the samples by constructing calibration curves with standard PQQ solutions of known concentrations, see Figure S3B. Knowing the sample volume (200 µL), the total amount of PQQ stripped-off from the surface immediately followed. The amount of GDH enzyme initially decorating the *fd*-particles was obtained

by multiplying the amount of PQQ by a factor of 2; each active GDH enzyme containing 2 PQQ molecules.

Control experiments for the PQQ assay method.

The presence of trace amounts of ferrocene dimethanol, mimicking the Fc-heads of the IgG-PEG-Fc present in the sample of stripped-off IgGs, were verified to not perturb the PQQ assay. We confirmed that reproducible calibration curves were obtained with standard PQQ solution freshly prepared, or heated to 50°C for 1h, showing that the thermal denaturation step of GDH did not degrade PQQ.

Starting with a standard solution of active (holo)-GDH, we verified that the 50°C, 1h thermal denaturation step resulted in > 97 % loss of enzymatic activity, accompanied by quantitative release of PQQ.

(IV) Estimating the concentration of ferrocene heads "seen" by the enzyme in the *fd*-scaffolded Fc-PEG wired PQQ-GDH assembly.

The high degree of spatial order of the immunological assembly on the *fd* scaffolds allows us to define the positions of the GDH and IgG-PEG-Fc hemispherical "layers" on the basis of the model represented in Figure S4A.
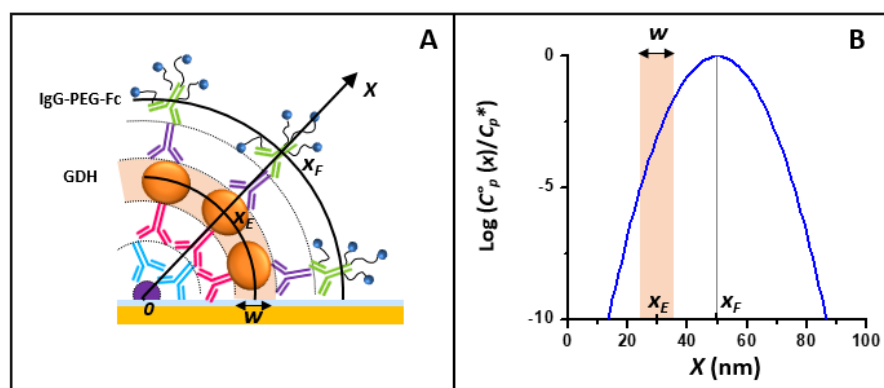
Figure S4. (A) Schematic representation of the *fd*-scaffolded integrated system. The orange shaded area corresponds to the domain where the redox site of the enzyme can be found. (B) Spatial distribution (i.e. concentration profile) of the Fc heads of the PEG chain as calculated by the elastic bounded diffusion model.

The GDH molecules are located a distance $X_E \sim 30$ nm away from the *fd* electrode contact (counting 5 nm for the *fd* radius and 10 nm per IgG layer). Due to the random orientation of GDH in the IgG-GDH conjugate, one can estimate that the active site of GDH can be found in a hemicylindrical region centered on X_E and displaying a width w of ~10 nm.

As shown in previous work,[7] the behavior of Fc-PEG chains attached to an IgG can be accurately modeled by the diffusion elastic model, where the spatial position of the Fc heads is dictated by two parameters: an apparent spring constant of the PEG chains, and the resting position of the Fc heads (defined as the position where the spring-like force is zero). It was shown that the resting position could be taken as corresponding to the center of the IgG-PEG-Fc layer, and an apparent molar spring constant

of $k_{spr} \sim 8.65 \; 10^{19}$ J mol^{-1} m^{-2} (or 0.14 pN/nm) was determined. In the present case, as depicted in Figure S4A it seems reasonable to take $X_F \sim 50$ nm as the resting positon of the Fc heads.

According to the model, the equilibrium spatial distribution (i.e. concentration profile) of the Fc heads is Gaussian and given by:

$$C_P^0(x) = C_p^* \exp\left[- k_{spr}(x - x_F)^2 / (2RT)\right]$$

With $C_p^* = \gamma_{Fc} \sqrt{k_{spr}/(2\pi RT)}$ and where γ_{Fc} is the Fc head coverage of the IgG-PEG-Fc layer, given here by the number of Fc-heads per virus ($N_{Fc} = 4000$) divided by the surface area, s, of the hemispherical IgG-PEG-Fc layer. This surface is given by $s \sim \pi L X_F$, with $L \sim 900$ nm the length of the decorated virus.

As in previous work,[8] we define the concentration of C_p^E seen by the enzyme as the average concentration in Fc –heads in the spatial region containing the redox site of the enzyme (orange shaded region in Figure S4), it is thus given by :

$$C_p^E = C_p^* / w \int_{x_{min}}^{x_{max}} \exp\left[- k_{spr}(x - x_F)^2 / (2RT)\right] dx$$

With $x_{max/min} = x_E +/- w/2$

Or more simply by: $C_p^E = \frac{\gamma_{Fc}}{2w}\left[erf(\lambda_{max}) - erf(\lambda_{min})\right]$ ES1

With $\lambda_{min/max} = \left(x_F - x_{max/min}\right)\sqrt{k_{spr}/(2RT)}$

Applying Equation ES1 yields to: $C_p^E = 12 \; \mu M$.

(V) Synthesis of the IgG-GDH conjugate.

1- Materials and Methods.

Reagents. Glucose, pyrroloquinoline quinone (PQQ), DCPIP (2,6-Dichloroindophenol sodium salt hydrate), phenazine methosulfate (PMS), dimethyl sulfoxide (DMSO), tris-(2-carboxyethyl)phosphine hydrochloride (TCEP), N-ethylmaleimide (NEM), 4-(N-maleimidomethyl)cyclohexane-1-carboxylic acid 3 sulfo-N-hydroxysuccinimide ester sodium salt (sulfo-SMCC), cysteamine and salts for buffer solutions (Tris-HCl, CaCl$_2$, MES, NaCl, (NH$_4$)$_2$SO$_4$ and phosphate buffered saline) were from Sigma-Aldrich. Succinimidyl 3-(2-pyridyldithio) propionate (SPDP) was from Thermo Scientific.

Anti-rabbit IgG (H+L) produced in goat (affinity isolated antibody, 2 mg/mL solution in 20 mM potassium phosphate, 0.15 M NaCl, pH 7.2) was from Sigma-Aldrich.

Plasmid pgp492 bearing the gene for soluble PQQ–GDH (sGDH) of *Acinetobacter calcoaceticus* was kindly provided by Dr Nicolas Mano (CCRP, University of Bordeaux, France).

Apo-GDH. *Production of apo-GDH.* *Escherichia coli* strain BL21(DE3) was transformed with pgp492,[9] and grown following a previously reported procedure.[10] Cells were harvested by centrifugation at 7500 *g* and 4°C for 15 min. The recovered pellet was resuspended at a 1:5 ratio (wt:vol) with lysis buffer (Tris HCl 20 mM pH 7.5 + 3mM CaCl$_2$) supplemented with one tablet/50ml of cOmplete™ EDTA-free Protease Inhibitor Cocktail (Roche).

The cell suspension was then subjected to 3 cycles of freeze/thaw by freezing in liquid nitrogen and then slowly thawed by incubation at room temperature in a water bath. Total cell lysis was performed by sonication with several 30 second pulses at 80W separated by a resting time of 30 s for a total duration of 15 min. The lysate was then centrifuged at 20000 *g* at 4°C for 1 h to pellet insoluble debris.

Purification of apo-GDH. The cleared lysate was loaded onto a SP Fast Flow sepharose column (GE Healthcare, Uppsala, Sweden) and purification was performed on an AKTA Purifier FPLC (Fast Protein Liquid Chromatography) chromatographic system (GE Healthcare, Uppsala, Sweden) with the Unicorn data system. Unbound proteins were washed from the column with 10 column volumes of binding buffer (Tris HCl 20 mM pH 7.5 + 3 mM CaCl$_2$), while bound GDH protein was eluted with the same buffer supplemented with 1 M NaCl. After collection, the eluted fractions were analyzed by SDS-Page electrophoresis (Mini-PROTEAN Tetra Cell (Biorad), colloidal coomassie blue staining). The thus identified GDH-containing fractions were pooled. After addition of (NH$_4$)$_2$SO$_4$ to a final concentration of 1.5 M, the pooled sample was applied on a butyl sepharose high performance column (GE Healthcare, Uppsala, Sweden). After washing with 10 column volumes of binding buffer (Tris HCl 20 mM pH 7.5 + 3 mM CaCl$_2$ + 1.5 M (NH$_4$)$_2$SO$_4$), the bound GDH was eluted with MES 20 mM buffer, pH 6.5. The GDH fractions identified by SDS-Page electrophoresis were pooled and then dialyzed overnight in Tris HCl 20 mM pH 7.5 + 3 mM CaCl$_2$ at 4°C to yield "purified" apo-GDH.

Holo-GDH (PQQ-GDH). *Reconstitution.* The holo-GDH (PQQ-GDH) was reconstituted from "purified" apo-GDH incubated with PQQ in excess as previously reported.[10,11] Unbound PQQ was removed by dialysis in Tris HCl 20 mM pH 7.5 + 3 mM CaCl$_2$ at 4°C. Incorporation of PQQ in holo-GDH was verified by UV-visible spectroscopy. The absorbance ratio at 338 nm and 280 nm, A$_{338}$/A$_{280}$, of reduced holo-GDH was used as an indicator for purity and cofactor content. Our preparations showed a ratio which falls in the reported range of 0.47-0.5.[10]

Purification by gel filtration chromatography. Before conjugation, it is of utmost importance that the dimeric holo-GDH is purified from traces of GDH monomers. This was achieved by gel filtration chromatography on a Superdex 200 increase 10/300 GL column (GE Healthcare, Uppsala, Sweden), using 0.1 M sodium phosphate pH 7.0 + 0.1 M NaCl as an eluent at a flow-rate of 0.5 mL/min. Concentration of Holo-PQQ-GDH (dimer, Mw 100.5 KDa) was determined at 280 nm with a specific absorption coefficient ε$_{280}$ of 1.8 L g^{-1} cm^{-1} (~180 000 M^{-1} cm^{-1}). To note the values published in the literature for the ε$_{280}$ coefficient of the holo-GDH, of 1.67 L g^{-1} cm^{-1},[12,10] and 1.92 L g^{-1} cm^{-1},[13].

2- Conjugating the holo-GDH and a goat anti-rabbit antibody (IgG).

Strategy. The preparation of antibody-enzyme IgG-GDH conjugate is based on SPDP/SMCC chemistries following the reaction scheme depicted in Figure S5: a modified antibody IgG with free (reduced) thiol, and a maleimide activated GDH enzyme are produced in parallel steps, by using SPDP /TCEP reducing agent, and sulfo-SMCC heterobifunctional activation-linking reagents respectively, and subsequently coupled in a final step via thiol-maleimide linking reaction to create a stable conjugate.
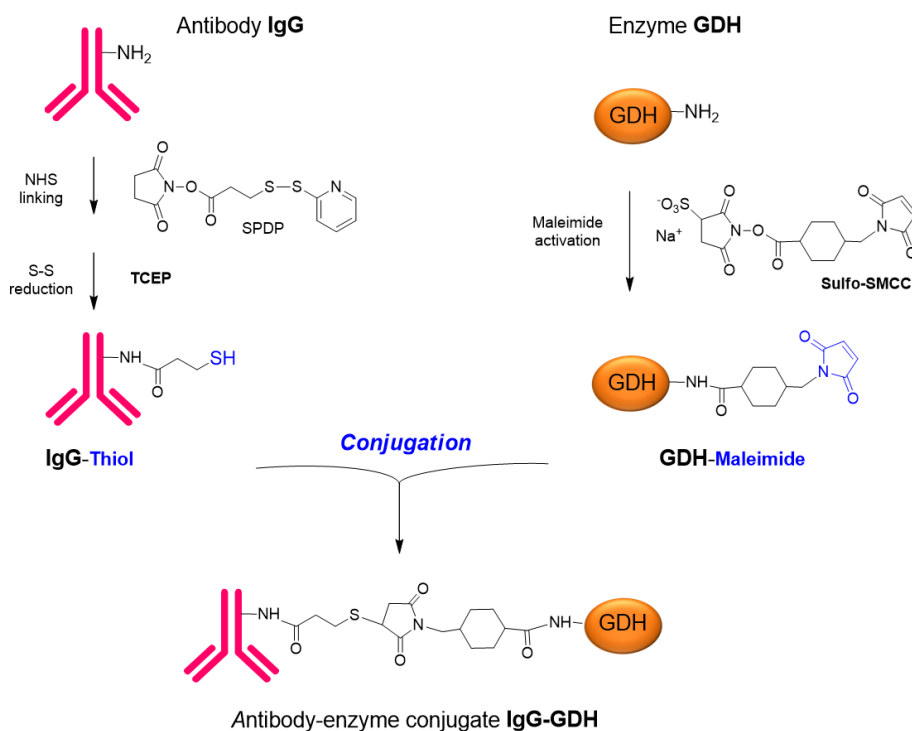
Figure S5. Reaction scheme for the preparation of antibody IgG–GDH enzyme conjugate using SPDP and SMCC heterobifunctional linker reagents. Both reagents are (N-hydroxysuccinimide (NHS) ester-activated at one end, and thus able to react with primary amino groups exposed on protein surface to form stable amide bonds. In this way, SPDP and SMCC cross-linkers are used respectively to add thiol groups on the IgG, and thiol-reactive maleimide groups on the GDH enzyme. Chemical coupling of the reduced thiolated IgG with maleimide-activated enzyme GDH thus creates antibody-enzyme conjugate IgG-GDH through the formation of a stable thioether bond.

IgG/GDH conjugation procedure (mg-scale). Our objective was to obtain the IgG-GDH antibody-enzyme conjugate as the 1:1 conjugate molecule (conjugate consisting of one antibody linked to one enzyme, molar ratio 1:1). This quality objective was set to ensure efficient immuno-immobilization of GDH, and preservation of the high enzyme activity after conjugation.

Our procedure for preparing the IgG-GDH conjugate was adapted from protocols using SPDP and SMCC chemistries outlining production of the 1:1 protein-protein conjugate (protein/protein molar ratio of 1:1), with minimal formation of multimer species.[14,15]

As detailed below, the procedure is run on a micromole scale in protein, and conjugation reaction of maleimide-activated GDH with thiol-IgG is performed at protein concentrations of ca. 10 µM in a GDH /IgG molar ratio close to 1 corresponding to that desired for the final conjugate.

I- Preparation of thiol-IgG and maleimide–activated GDH sample solutions.

(a) <u>Conditioning the IgG and GDH samples before activation</u>.

Before SPDP activation, 150 µL of the commercial solution of goat anti-rabbit antibody IgG (~0.3 mg) were transferred in a Vivaspin 500 centrifugal filter device (10 kDa) for buffer exchange with reaction buffer PBS (0.1 M sodium phosphate pH 7.5, 0.1 M NaCl) down to a final sample volume of ~100 µL. *Before sulfo-SMCC activation*, 170 µL (~0.2 mg) of enzyme holo-GDH solution (prepared this work, 1.2 mg/mL) were transferred in a Vivaspin 500 centrifugal filter device (10 kDa), to bring (after 3 centrifugations at 15 000 g, 10 °C) the GDH sample solution volume down to ~100 µL in PBS.

Concentrations of the 100-µL IgG and GDH samples in PBS were then checked before activation by spectrophotometric absorbance measurement at 280 nm in a microplate (0.28 cm path length), and using specific absorption coefficients at 280 nm of 1.37 L g^{-1} cm^{-1} for IgG (Mw 147 kDa), and 1.8 L g^{-1} cm^{-1} for (holo-GDH (dimer, Mw 100.5 kDa)).

(b) <u>Chemical activations of the IgG and GDH samples</u>

Thiol-IgG and maleimide-activated GDH samples were prepared in parallel for immediate mixing.

* *Preparation of the thiol-IgG sample.* For the thiolation of IgG, the SPDP reagent was used in a 5-molar excess compared to protein. An aliquot of a SPDP solution « immediately prepared » in anhydrous DMSO, was rapidly added to the 100-µL IgG protein (~20 µM) solution in PBS while stirring. The coupling reaction was carried out for 1 h at room temperature RT (21-25 °C) protected from light. Any excess of reagent and reaction products of low relative molecular mass were removed by using a microspin desalting resin column Zeba (Thermo Scientific supplier 7K). The antibody-bound disulfide groups were then reduced to free thiol groups by incubation with TCEP reducing agent used in a ~5-fold molar excess/protein (an aliquot of a freshly prepared TCEP solution in PBS, final 0.1 mM). After 15 min incubation at RT, the thiol–IgG protein solution is ready to be combined with the maleimide–GDH solution.

* *Preparation of the maleimide–activated GDH sample*. For the maleimide activation of GDH, the sulfo-SMCC reagent was used in a 10-molar excess compared to protein. An aliquot of a sulfo-SMCC solution, « immediately prepared » in water, was rapidly added to the 100-µL GDH (20 µM) enzyme solution in PBS while stirring. The coupling reaction was carried out for 1h at RT, protected from light. The maleimide-activated GDH was then purified from excess sulfo-SMCC and by-products using a microspin desalting column Zeba. The thus prepared maleimide IgG protein solution (kept on ice) is then ready to be combined with the thiol–IgG solution.

II- Producing the IgG-GDH conjugate by reacting thiol–IgG and maleimide–GDH enzyme.

The thiol-IgG and maleimide-GDH protein sample solutions were mixed (total volume, ~200 µL; ~10 µM in each protein) and conjugated for 1h30 at RT protected for light. After NEM capping (0.2 mM, 20 min RT) of remaining free thiols, followed by cysteamine capping (0.1 mM, 20 min RT) of remaining free maleimides, the IgG-GDH conjugate mixture was subjected to gel filtration purification.

III- Isolation/characterization of the IgG-GDH conjugate.

Gel filtration chromatography. The IgG-GDH 1:1 conjugate was isolated by gel filtration chromatography separation of the 200µL-crude reaction mixture (proteins mg-scale) in a single run on Superdex 200 Increase 10/300 GL. Figure S6 highlights the high column selectivity for the separation of the IgG and GDH enzyme reactants scaled at mg quantities, and Figure S7 presents a chromatogram characterizing a typical separation of the IgG-GDH 1:1 conjugate product from reaction-mixture components of larger and lower size on the Superdex.
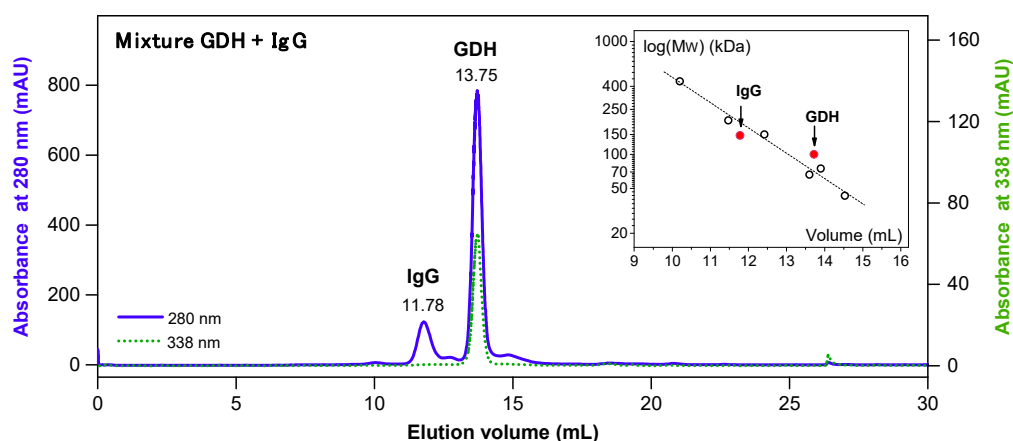
Figure S6. Gel filtration chromatography separation of IgG and holo-GDH proteins on Superdex 200 Increase 10/300 GL. Chromatogram of a 100 µL-mixture containing 1 mg of purified holo-GDH enzyme (this work) and 0.35 mg of a commercial goat antibody IgG, with monitoring at 280 nm (intended to detect protein) (blue solid trace) and 338 nm (intended to detect protein bound-PQQ) (green dotted trace). Inset. Known molecular weight Mw in the log scale *versus* elution volume. Standard globular proteins (GE Healthcare kit) are plotted as open circles (o). As can be seen, the data points display some dispersion around the regression "calibration" line (dotted trace) . IgG (150 kDa) and holo-GDH (dimer, 100.5 kDa) proteins are plotted as filled circles (●). It is seen that GDH and IgG proteins lie slightly outside the standards curve. Selected standards (GE Healthcare kit): ferritin (440 kDa), b-amylase catalase (200 kDa), alcohol dehydrogenase (150 kDa), conalbumin (75 kDa), BSA (66 kDa), ovalbumin (43 kDa). Averaged data over 2 runs. Mobile phase: PBS eluted at a flow-rate of 0.5 mL/min.

☞ As shown in Figure S6, the two proteins, holo-GDH enzyme (dimer, Mw 100.5 kDa) and IgG antibody (Mw 147 kDa), eluted as well-separated peaks. The IgG and GDH peak elution volumes were reported in a "calibration curve" relating molecular weight Mw (log scale) to elution volume established for selected globular protein standards (GE Healthcare kit) (Fig. S6, inset plot). It appeared that GDH and IgG proteins were not strictly separated on the basis of their molecular size, deviating from a globular shape expectation. Holo-GDH eluted earlier, with an estimated apparent decrease of its molecular weight of ca. 25 kDa. This mass-deviation-decrease for holo-GDH on Superdex (pointing GDH dimer as a protein with an apparent Mw 70-75 kDa) was already observed, and described by Olsthoorn and Duine[10] as an anomalous hydrodynamic behavior. Goat IgG protein eluted sligthly later than expected from the standard curve, with an apparent mass of 170-180 kDa, which indicates that IgG may be somewhat elongated as already reported.[16,17]

From these observations, the 1:1 IgG-GDH conjugate protein (calculated Mw 250 kDa) features a molecule composed of two-non globular proteins, predicted to deviate from the standard globular behavior, but confidently expected to elute in a ca. 1-mL volume (Mw ~220-280 kDa) before IgG peak.

☞ As shown in Figure S7, the IgG-GDH conjugate was eluted at 10.82 min, as a peak right before the unconjugated IgG, with an efficient separation of a ca. 1-mL volume, meeting our expectations and predictions.

In the inset plot of Figure S7, the IgG-GDH peak elution volume is reported with a calculated Mw 250 kDa (= sum of Mw IgG and Mw GDH) in a said "calibration curve" relating the logarithm of the molecular weight Mw *vs.* elution volume. It can be observed that the curve derived for IgG, GDH, and IgG-GDH conjugate exhibits a slope (inset, red solid line) less steep than the curve for globular proteins (inset, dotted line). As claimed by Shimazu.com commenting gel filtration (= size exclusion SEC) "calibration curves": "*The lower the slope of the calibration curve, the larger the difference in elution volume between small differences in molecular weight*". In our case, the less sloped curve obtained for our "non globular" proteins provided a real benefit for a more accurate chromatographic separation.
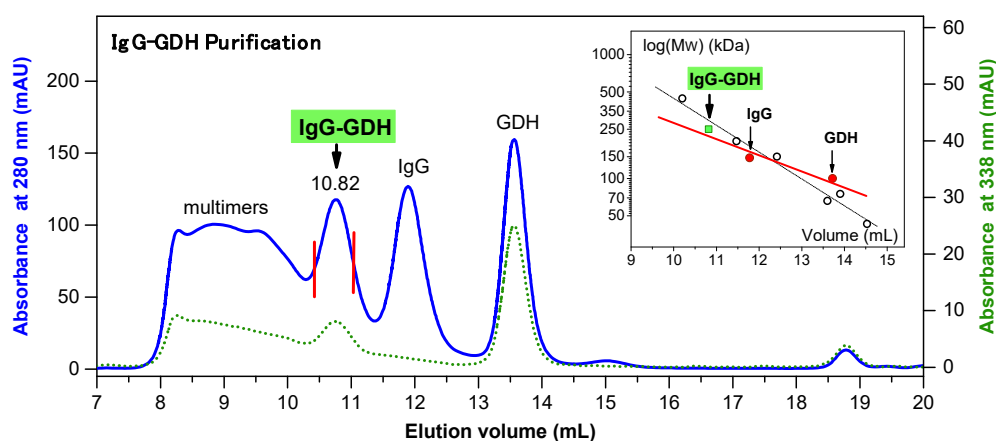

Figure S7. **Gel filtration chromatogram of a IgG/GDH conjugation reaction mixture** showing the separation of IgG–GDH 1:1 conjugate (peak elution volume, 10.82 mL) from larger proteins (multimers), and smaller unconjugated IgG and GDH protein molecules on Superdex 200 Increase 10/300 GL. Fractions of IgG-GDH were collected from the narrow selected region delimited by the vertical red lines. Inset. The elution volume of IgG-GDH molecule is reported in the log Mw *vs.* volume plot (described in the legend of Fig. S6), as a filled green square (■), with an assigned Mw of 250 kDa expected for a molecule containing one IgG moiety (known Mw, 150 kDa) + one GDH moiety (known Mw, 100 kDa). The drawn solid linear red line, simulating a possible "calibration curve" for IgG, GDH and IgG-GDH molecules, exhibits a less steep slope than the "standard globular" curve. Absorbance detection at 280 nm (solid —) and 338 nm (short dotted ····). Mobile phase: PBS eluted at a flow-rate of 0.5 mL/min. Injected volume: 200 μL. Total load in proteins: ~ 0.5 mg.

All our IgG-GDH samples were isolated from collected fractions eluted in a narrow ~0.5 mLvolume range such as the one typically delimited by the red vertical lines apart the peak in Figure S7.

IgG-GDH once collected was characterized by Uv-vis (see below), and then typically stored at a concentration of ~50 μg/mL in PBS containing 0.1% BSA in the fridge.

Spectral properties of our IgG-GDH conjugate samples.

Figure S8 (curve a) shows a typical UV-visible absorption spectrum for a IgG-GDH collected sample from gel filtration chromatography. The spectrum of IgG-GDH shows a "protein-type" absorption band with a maximum around 280 nm, and a large band around 350 nm due to "protein-bound PQQ".
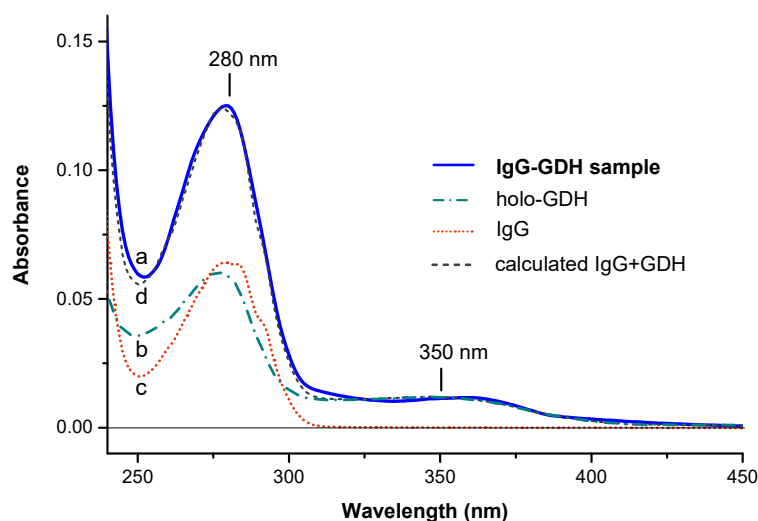

Figure S8. **Absorption spectra of IgG-GDH conjugate, holo-GDH, and IgG proteins**. (a) Spectrum of the purified IgG-GDH conjugate solution used in this work (solid blue). (b) Spectrum of a ~ 0.34 µM (~ 0.34 mg/mL) solution of active holo-GDH (dash dotted green) in PBS. (c) Spectrum of a ~0.32 µM (~ 0.47 mg/mL) solution of goat IgG (dotted red) in PBS. (d) Calculated spectrum = 1x(b)+1x(c) sum (short dashed grey), mimicking the absorbance profile expected for a solution containing IgG and active holo-GDH in an approximate GDH/IgG molar ratio of 1:1 (0.34/(0.32), at a ca. 0.3 µM concentration. As noted, the calculated profile nicely reproduces the experimental spectrum of our IgG-GDH sample. As proposed in text, the A_{280}/A_{350} absorbance ratio can be used as a convenient control indicator for quality of our IgG-GDH samples. PBS buffer. 1 cm path length.

☞ Determination of the ratio of spectrophotometric absorbance of the IgG-GDH sample at 280 nm to that of 350 nm, A_{280}/A_{350}, was shown to provide a quick evaluation of the IgG/GDH molar ratio as commented below :

Based on known epsilon (280, and 350 nm) and masses of the GDH and antibody IgG species, it is proposed therein that undertermined GDH/ IgG molar ratio for a IgG-GDH conjugate is given by the formula:

$$\text{Molar ratio GDH/IgG} = \frac{6}{(A_{280}/A_{350} - 5.5\,)}$$

Actually, we noted for all our conjugate preparations, that the experimental A_{280}/A_{350} ratio showed a nearly constant 8-10 value. This value according to the formula gives for our IgG-GDH samples, a molar ratio varying between 1.0 to 1.1.

REFERENCES

(1) Reeves, J. H.; Song, S.; Bowden, E. F. Application of Square Wave Voltammetry to Strongly Adsorbed Quasireversible Redox Molecules. *Anal. Chem.* **1993**, *65*, 683–688.

(2) Bourdillon, C.; Demaille, C.; Moiroux, J.; Savéant, J.-M. Step-by-Step Immunological Construction of a Fully Active Multilayer Enzyme Electrode. *J. Am. Chem. Soc.* **1994**, *116*, 10328–10329.

(3) Witarto, A. B.; Ohtera, T.; Sode, K. Site-Directed Mutagenesis Study on the Thermal Stability of a Chimeric PQQ Glucose Dehydrogenase and Its Structural Interpretation. *Appl. Biochem. Biotechnol. - Part A Enzym. Eng. Biotechnol.* **1999**, *77*, 159–168.

(4) Matsushita, K.; Ameyama, M. [24] d-Glucose Dehydrogenase from Pseudomonas Fluorescens, Membrane-Bound. In *Methods in Enzymology*; Academic Press, 1982; pp 149–154.

(5) An, R.; Moe, L. A. Regulation of Pyrroloquinoline Quinone-Dependent Glucose Dehydrogenase Activity in the Model Rhizosphere-Dwelling Bacterium Pseudomonas Putida KT2440. *Appl. Environ. Microbiol.* **2016**, *82*, 4955–4964.

(6) Zhang, L.; Miranda-Castro, R.; Stines-Chaumeil, C.; Mano, N.; Xu, G.; Mavré, F.; Limoges, B. Heterogeneous Reconstitution of the PQQ-Dependent Glucose Dehydrogenase Immobilized on an Electrode: A Sensitive Strategy for PQQ Detection down to Picomolar Levels. *Anal. Chem.* **2014**, *86*, 2257–2267.

(7) Anne, A.; Demaille, C.; Moiroux, J. Elastic Bounded Diffusion. Dynamics of Ferrocene-Labeled Poly(Ethylene Glycol) Chains Terminally Attached to the Outermost Monolayer of Successively Self-Assembled Monolayers of Immunoglobulins. *J. Am. Chem. Soc.* **1999**, *121*, 10379–10388.

(8) Anicet, N.; Anne, A.; Bourdillon, C.; Demaille, C.; Moiroux, J.; Savéant, J. M. Electrochemical Approach to the Dynamics of Molecular Recognition of Redox Enzyme Sites by Artificial Cosubstrates in Solution and in Integrated Systems. *Faraday Discuss.* **2000**, *116*, 269–279.

(9) Cleton-Jansen, A.-M.; Goosen, N.; Vink, K.; van de Putte, P. Cloning, Characterization and DNA Sequencing of the Gene Encoding the Mr50000 Quinoprotein Glucose Dehydrogenase FromAcinetobacter Calcoaceticus. *Mol. Gen. Genet. MGG* **1989**, *217*, 430–436.

(10) Olsthoorn, A. J. J.; Duine, J. A. Production, Characterization, and Reconstitution of Recombinant Quinoprotein Glucose Dehydrogenase (Soluble Type; EC 1.1.99.17) Apoenzyme OfAcinetobacter Calcoaceticus. *Arch. Biochem. Biophys.* **1996**, *336*, 42–48.

(11) Durand, F.; Limoges, B.; Mano, N.; Mavré, F.; Miranda-Castro, R.; Savéant, J. M. Effect of Substrate Inhibition and Cooperativity on the Electrochemical Responses of Glucose Dehydrogenase. Kinetic Characterization of Wild and Mutant Types. *J. Am. Chem. Soc.* **2011**, *133*, 12801–12809.

(12) Flexer, V.; Durand, F.; Tsujimura, S.; Mano, N. Efficient Direct Electron Transfer of PQQ-Glucose Dehydrogenase on Carbon Cryogel Electrodes at Neutral PH. *Anal. Chem.* **2011**, *83* (14), 5721–5727.

(13) Olsthoorn, A. J. J.; Duine, J. A. On the Mechanism and Specificity of Soluble, Quinoprotein Glucose Dehydrogenase in the Oxidation of Aldose Sugars. *Biochemistry* **1998**, *37*, 13854–13861.

(14) Scientific, T. F. Protein–Protein Crosslinking Kit.

(15) Hermanson, G. T. *Bioconjugate Techniques*, 3rd Ed.; Academic Press, 2013.

(16) Armstrong, J. K.; Wenby, R. B.; Meiselman, H. J.; Fisher, T. C. The Hydrodynamic Radii of Macromolecules and Their Effect on Red Blood Cell Aggregation. *Biophys. J.* **2004**, *87*, 4259–4270.

(17) Smilgies, D.-M.; Folta-Stogniew, E. Molecular Weight–gyration Radius Relation of Globular Proteins: A Comparison of Light Scattering, Small-Angle X-Ray Scattering and Structure-Based Data. *J. Appl. Cryst.* **2015**, *48*, 1604–1606.